AGU100 ADVANCING EARTH AND SPACE SCIENCE

Response of a Rheologically Stratified Lithosphere to Subduction of an Indenter-Shaped Plate: Insights Into Localized Exhumation at Orogen Syntaxes

Alexander Koptev[1] (iD), Todd A. Ehlers[1] (iD), Matthias Nettesheim[1] (iD), and David M. Whipp[2] (iD)

[1]Department of Geosciences, University of Tübingen, Tübingen, Germany, [2]Department of Geosciences and Geography, University of Helsinki, Helsinki, Finland

Abstract This study investigates the influence of the 3-D geometry of a down-going plate, the rheological structure of the upper plate, and the migration of the overriding plate toward the trench in relation to the overall subduction velocity on the exhumation pattern in orogen syntaxes. Using a thermomechanical numerical code (DOUAR), we analyze the strain localization, rock uplift, and exhumation response of a rheologically stratified continental lithosphere to subduction of a convex-upward-shaped indenter. The models consider three thermorheological lithospheric profiles that determine the degree of mechanical coupling between the upper crust and lithospheric mantle. These models include a strong, cratonic lithosphere; a weaker, younger (and hotter) continental plate; and an intermediate case. The strongly coupled case predicts a localization of high rock uplift rates along narrow linear bands crossing the entire model domain parallel to the trench. In contrast, in a weakly coupled lithosphere, rock uplift is concentrated within a curved ellipse region of anomalously high exhumation rates located above the indenter apex. The aspect ratio of the localized area of rapid rock uplift is controlled by the initial width of the rigid indenter and the relationship between boundary velocities. In particular, the combination of little or no upper plate migration with a narrow indenter causes a nearly circular region (~100-km diameter) of rapid exhumation that resembles the pattern of thermochronometer ages observed in orogen syntaxes such as the Southeast Alaska and the Olympic Mountains of the Cascadia subduction zone (western USA).

1. Introduction

The transition between adjacent subduction segments at plate corners represents an important type of tectonic setting (Figure 1). Recent observational (Hayes et al., 2012) and modeling studies (Mahadevan et al., 2010) show that 3-D bending at plate corner locations (Figures 1b–1d) required by subduction on a spherical Earth leads to geometric stiffening at the ends of subduction arcs producing a convex-upward-shaped bump of the subducting plate referred to hereafter as a "flexural bulge" or "indenter" (Figure 1a). The relatively narrow regions above these convex bends—termed "orogen syntaxes" or "syntaxial orogens" (cf. Bendick & Ehlers, 2014)—separate the longer straight plate boundaries.

Orogen syntaxes have attracted attention over recent years because they contain some of the most rapid rock exhumation rates (>5 mm/year) observed. This extreme exhumation is characterized by a circular (~100+-km diameter) zone of rock uplift (also dubbed a "bull's-eye" pattern, Bendick & Ehlers, 2014). Classical examples of strong bull's-eye spatial localization of rock uplift include regions such as the Southeast Alaska (Enkelmann et al., 2010; Falkowski et al., 2014; Koons et al., 2010), the Olympic Mountains in Washington State, USA (Brandon et al., 1998; Michel et al., 2018; Pazzaglia & Brandon, 2001), and Nanga Parbat and Namche Barwa in the Himalayan syntaxes (Crowley et al., 2009; Enkelmann et al., 2011; Lang et al., 2016; Zeitler et al., 2001, 2014).

Koons et al. (2002, 2013) showed that locally enhanced erosion rates can lead to focused exhumation through significantly reduced crustal strength caused by thermal weakening (the model dubbed a "tectonic aneurysm"—see also Zeitler et al., 2001, 2014). Their approach, however, does not account for the internal 3-D geometry of subducting plates while approximating the subsurface to be of homogeneous composition with straight-lined boundaries. Such geometric simplification is permissible for many parts of subduction zones but at the transition between adjacent plate boundary segments the impact of the 3-D configuration of the subducting lithosphere may be important. To investigate these 3-D geometric complexities Bendick and Ehlers (2014) applied a numerical model focused on the variations in shape of the 3-D down-going
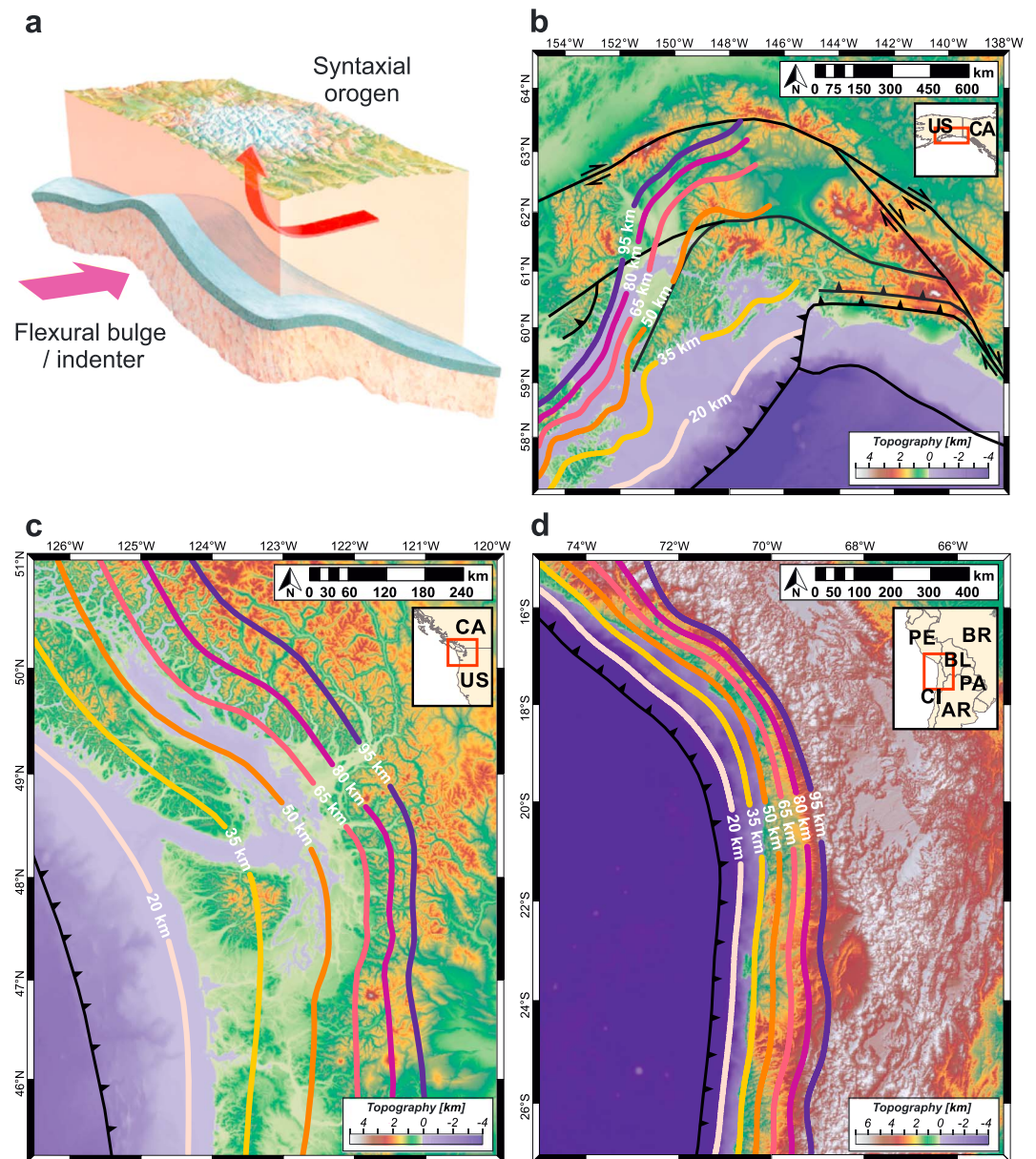
Figure 1. (a) Schematic representation for the flexural bulge of the subducting slab at the plate corner and syntaxial orogen above (modified from Bendick & Ehlers, 2014). (b–d) Observed subducting plate geometry in the plate corner locations (slab contours from the global 3-D model of subduction zones geometry by Hayes et al., 2012): (b) the Southeast Alaska (the major faults after Koons et al., 2010), (c) the Olympic Mountains of the Cascadia subduction zone, and (d) the South American subduction zone. The South American subduction zone is characterized by a moderate slab curvature comparing to the Southeast Alaska and the Cascadia subduction zone.

plate and its role in overriding plate deformation and rock exhumation. They found that rapid vertical uplift and exhumation can be localized into a bull's-eye region in response to a flexural bulge on the down-going plate. However, the rheological structure adopted in their work was simplified and allowed only for purely viscous deformation. Their approach also excluded the effects of brittle strain localization in the overriding plate that might be critical for the resulting strain and topographic evolution of the region (see, e.g., Vogt et al., 2017, 2018).

In recent decades, advances have been made to better understand the role of rheological stratification of the lithosphere (Burov, 2011; Ranalli & Murphy, 1987) on deformation and rock exhumation in convergent orogens. This has been done by means of analogue (e.g., Willingshofer et al., 2013) and numerical modeling

(e.g., Burov et al., 2001; Erdos et al., 2014; Jammes & Huismans, 2012; Vogt et al., 2017, 2018). In view of these advances, the subduction of a down-going plate with a convex-upward-shaped indenter (as investigated by Bendick & Ehlers, 2014) has been further explored (Nettesheim et al., 2018) with a series of numerical thermomechanical experiments assuming a viscoplastic rheology and stratification of the overriding continental lithosphere. In these models, the highest rock uplift rates are localized within elongated areas above both the indenter bulge and straight segments of the subducting plate and thus not reproducing the observed concentric bull's-eye pattern of vertical uplift as described in Bendick and Ehlers (2014) and observed in some syntaxial orogens. Here we build upon the work of Nettesheim et al. (2018) with particular focus on variations in the style of deformation and associated rock uplift in syntaxial orogens as a function of the degree of rheological (de)coupling of the upper plate (see, e.g., Brun, 2002; Koptev et al., 2018; Tetreault & Buiter, 2018). In contrast to the work of Nettesheim et al. (2018) who focused on the effect of variable velocity boundary conditions and erosion mechanisms, we investigate the effect of different thermorheological lithospheric profiles ranging from mechanically decoupled to completely coupled by varying the lithology of the lower crust and the initial crustal geotherm in order to identify the role of rheological structure on the spatial localization of rock uplift. Similar to Nettesheim et al. (2018), we have also tested different contributions in the total shortening by subduction of the down-going plate and migration of the overriding plate toward the trench (Capitanio et al., 2010; Heuret & Lallemand, 2005; Schellart et al., 2007) through the introduction of variable rates of upper plate advance (V_{Adv}) that refers to the relation between boundary velocities applied at the opposite sides of the model. Finally, given the large uncertainty in seismic images of subducting plate geometries, various configurations of the flexural bulge geometry are also investigated here.

In this study, we compare our modeling results to natural settings; however, it is beyond the scope of this study to reproduce the detailed structure of observed deformation and rock uplift in any particular orogen syntax. At the current stage, this is not feasible due to the lack of available information on the lateral heterogeneity of the overriding lithosphere as well as indenter geometry and properties. In contrast, our main objective here is to quantify the general consequences of subduction of a flexural bulge underneath rheologically stratified continental lithosphere. For this purpose, we first investigate the influence of overriding lithosphere rheological profiles (strength envelopes) on the resulting pattern of strain localization and associated rock uplift. We follow this by a comparison of our model inferences with observed exhumation rates in the Southeast Alaska, the Olympic Mountains of the Cascadia subduction zone (western USA), and the South American subduction zone.

2. Methods

2.1. Model Design

The numerical simulations presented here were conducted using DOUAR (Braun et al., 2008; Thieulot et al., 2008), a three-dimensional finite element code designed to solve the Stokes and heat transfer equations. See the numerical methods section in supporting information for governing equations and material properties used in the model, and additional details. We also refer readers to Braun and Yamato (2010), Whipp et al. (2014) and Nettesheim et al. (2018) for further information.

The model setup encompasses an area of horizontal dimensions 800 km × 800 km with a thickness of 80 km (Figure 2a) using a 3-D box with 128 × 128 × 52 elements, resulting in a grid spacing of 6.25 and 1.54 km in horizontal and vertical directions, respectively.

Our model setup closely resembles that of Nettesheim et al. (2018): The internal model structure corresponds to a simplified two-block system that can be applied to both continental and oceanic collisional settings: a rigid wedge-shaped subducting plate with a central convex-upward-shaped bulge and a rheologically layered overriding lithosphere (Figure 2a). The background sections of the subducting plate have a minimum depth of 50 km at $y = 0$ km that gradually increases up to the slab termination at $y = 320$ km. In contrast, the indenter geometry is characterized by a 30-km minimum depth, termination at $y = 400$ km and lateral (along-strike) width varying from 450 to 150 km. The indenter width in the x direction is one of the variables explored in our study (see Figure 2b3 and Table 1). The overriding plate corresponds to a laterally homogeneous three-layered continental lithosphere composed of a 40-km-thick mantle overlain by the continental crust equally divided into upper (20 km) and lower crust (20 km).
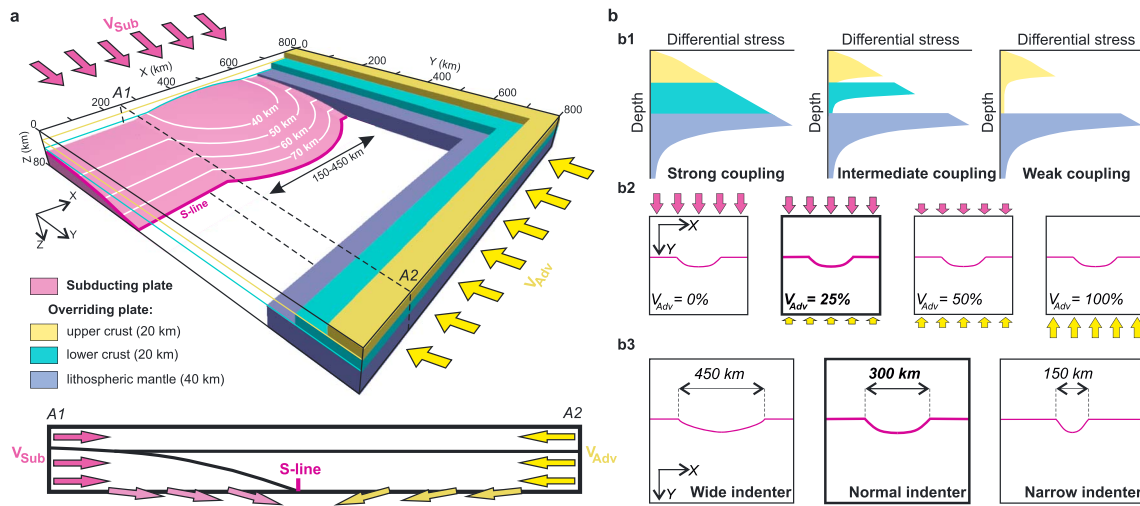
Figure 2. (a) Three- dimensionalview of modeling domain: a rheologically layered overriding lithosphere and a rigid subducting plate containing a central convex-upward-shaped bulge (indenter) and a background (i.e., nonindenter) portion. S line refers to intersection of the down-going plate with the model bottom plane; violet and yellow arrows show subduction (V_{Sub}) and upper plate advance (V_{Adv}) components of the shortening, respectively. Schematic vertical cross section: Horizontal velocities are directed along y axis with V_{Sub} and V_{Adv} to the left and right of the S line, respectively; vertical material outflux through the lower boundary is linearly increased from the model sides to the S line. (b) Key variable parameters: (b1) rheological structure of the overriding plate (from left to right): strong, intermediate, and weak coupling between the upper crust and lithospheric mantle; (b2) velocity boundary conditions (from left to right): 0%, 25%, 50%, and 100% of the upper plate advance in the total shortening rate; and (b3) width of the indenter (from left to right): 450, 300, and 150 km. The reference values of upper plate advance and indenter width (25% and 300 km, respectively) are highlighted by thick-line slots on b2 and b3.

Table 1
Experiments: Key Variable Parameters and Results

	Model parameters					Resulting aspect ratio of the isolated zone of rapid exhumation (if applicable[e])	
	Properties of the overriding lithosphere						
N	Lower crust composition[a]	Initial geotherm[b]	Rheological coupling[c]	Upper plate advance (V_{Adv})[d]	Indenter width (km)		Figures
1	mafic	"cold"	strong	25%	300	—	3, 6a, and S1
2	mafic	"normal"	intermediate	25%	300	—	4, 6b, andS2
3	felsic	"normal"	weak	25%	300	~1:4	5, 6c, S3, and 8b
4	felsic	"normal"	weak	0%	300	~1:3	7a, S4a, and S5
5	felsic	"normal"	weak	50%	300	—	7b, S4b, and S6
6	felsic	"normal"	weak	100%	300	—	7c, S4c, and S7
7	mafic	"cold"	strong	25%	150	—	S8a
8	mafic	"normal"	intermediate	25%	150	—	S8b
9	felsic	"normal"	weak	25%	150	~1:2	8c and S8c
10	felsic	"normal"	weak	25%	450	~1:6	8a
11	felsic	"normal"	weak	0%	150	~1:1.5	9a, 10a, S9 and S10, and S11c
12	felsic	"normal"	weak	50%	150	—	9b
13	felsic	"normal"	weak	100%	150	—	9c
14	mafic	"cold"	strong	0%	150	—	S11a
15	mafic	"normal"	intermediate	0%	150	—	S11b

[a]Mafic and felsic lower crust compositions refer to wet granite and dry diabase flow laws, respectively. [b]"Normal" initial geotherm is defined with taking into account crustal heat generation (see Table S1) whereas "cold" one corresponds to the models without radiogenic heat production. [c]Rheological coupling of the overriding plate is controlled by the lower crust composition and initial geotherm (see explanation in the section 2.2). [d]Upper plate advance (V_{Adv}) represents the contribution of the boundary velocity applied at the right side of the model box in the total shortening rate (see Figure 2a and explanation in the section 2.1). [e]Aspect ratio is indicated only for the cases when high exhumation rates are concentrated within the single curved ellipse region above the indenter bulge.

To identify the effect of a subducting indenter on the deformation pattern in the rheologically stratified upper plate, we follow the established approach of numerical (e.g., Cailleau & Oncken, 2008; Iwamori et al., 2007; Ruh et al., 2016; Wada et al., 2008) and analog (e.g., Buttles & Olson, 1998; Kincaid & Griffiths, 2003) modeling. We intentionally simplify our model by prescribing that the down-going plate (including indenter bulge) remains a rigid and undeformed mass and keeps its initial configuration through the entire model history. This approach precludes mass transfer between the subducting and overriding plates to ensure mass balance at every time step. While the rheology of the down-going plate is purely viscous at 10^{25} Pa·s, we additionally include a thin (3–4 km thick) and weak (a constant viscosity of 10^{19} Pa·s) layer on top in order to reduce its internal deformation as well (e.g., Willingshofer & Sokoutis, 2009). Despite this simplification, we expect general insights into the dominant controls on the tectonics of the upper plate to remain valid for the uppermost segment of the lithosphere-mantle system (0–80 km), given that most of internal slab deformation usually occurs at much greater depths (see, e.g., Gerya et al., 2004).

The upper plate (see Table S1) is modeled as a rheologically stratified continental lithosphere with an alternation of brittle and ductile layers. The viscous rheology of the felsic upper crust is described by a wet granite flow law (Carter & Tsenn, 1987) in all experiments. For the lower crust, we consider two different ductile flow laws—wet granite flow law (felsic lower crust) or dry diabase flow law (mafic lower crust)—in different experiments (see Table S1) in order to explore different levels of mechanical (de)coupling between the upper crust and the mantle lithosphere (e.g., Brun, 2002; Brun et al., 2018; Gueydan et al., 2008; Koptev et al., 2015, 2016; Koptev et al., 2018). The viscous rheology of the mantle is controlled by the flow law that conforms to the known deformation of olivine aggregates (Hirth & Kohlstedt, 2003; Jadamec & Billen, 2012). Brittle behavior is modeled by a Mohr-Coulomb failure criterion. In the upper and lower crust, this includes a linear reduction in the friction angle with increasing accumulated strain (linear strain softening; see, e.g., Huismans & Beaumont, 2002). For the lithospheric mantle, however, the coefficient of internal friction of the Mohr-Coulomb failure criterion remains strain independent (Table S1).

At the left ($y = 0$ km) and right ($y = 800$ km) sides of the model box, we apply kinematic boundary conditions of uniform and time-independent boundary velocities parallel to the y axis that define the material influx resulting in lateral shortening accommodated by subduction (V_{Sub}) or/and migration of the overriding plate toward the subducting plate referred below as "upper plate advance" (V_{Adv}), respectively (Figure 2a). The velocity boundary condition at the front ($x = 0$) and back ($x = 800$ km) sides are free slip. Conservation of mass is ensured by material outflux through the lower ($z = 80$ km) boundary. The upper surface remains flat from erosion that instantly removes all material uplifted above the initial surface elevation so that modeled near-surface vertical (rock uplift) velocities are equal to rock exhumation rates (England & Molnar, 1990). The relation between boundary velocities applied at the left (V_{Sub}) and right (V_{Adv}) model sides represents a variable parameter of this study (see section 2.2 and Table 1). Total shortening rate ($V_{Tot} = V_{Sub} + V_{Adv}$), however, remains the same ($V_{Tot} = 30$ mm/year) in all experiments.

Initial "normal" nonlinear steady state geotherm is defined by boundary temperatures of 0 °C and 930 °C at the top ($z = 0$ km) and the bottom ($z = 80$ km) while taking into account heat production in the upper and lower crust (see Table S1 for parameters). This setup results in a geothermal gradient at the model surface of 27 °C/km, which decreases to 13 °C/km at the boundary between upper and lower crust and finally to 8 °C/km from the Moho downward. In contrast, models with no radiogenic heat generation in the crust result in linear temperature distribution with the constant geothermal gradient of 11.6 °C/km referred here as a "cold" initial geotherm (see Table S1). We apply insulating boundary conditions (zero conductive heat flux) for all vertical sides.

Predicted cooling ages are calculated using the time-temperature history of tracer particles within the model domain (see Braun, 2003; Ehlers, 2005; Whipp et al., 2009, for underlying principles and Nettesheim et al., 2018, for this specific implementation). We calculate apatite fission track (AFT) ages (referred below as "AFT-predicted ages") that indicate the time since an apatite grain has cooled below ~90–120 °C. We focus on this thermochronometer system because AFT measurements have been applied widely to quantify exhumation rates in the orogens we compare our model results to.
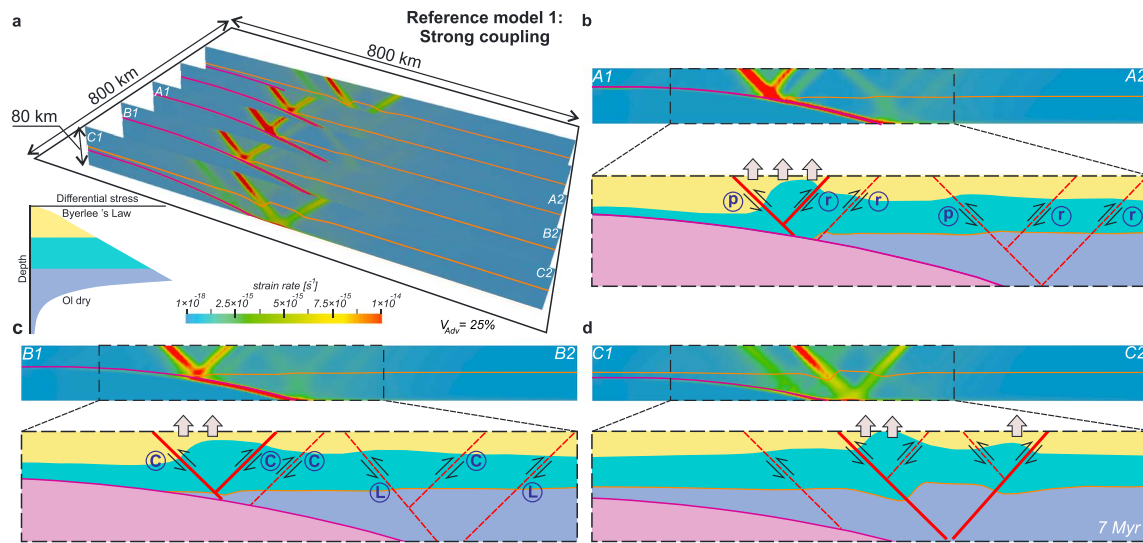
Figure 3. Reference experiment for strong rheological coupling of the overriding lithosphere (model **1**) after 7-Myr modeling time. (a) Three-dimensional view of the second invariant of strain rate tensor. (b–d) Vertical cross sections parallel to y axis with schematic interpretations for their central segments. The layer colors are as in Figure 2. The violet and orange lines refers to subducting plate and Moho interfaces, respectively. The red lines on the interpretation profiles represent the shear zones—the planes of stronger (solid lines) or weaker (dashed lines) localized high strain rate intensity ($>8 \times 10^{-15}$ 1/s and $>3-6 \times 10^{-15}$ 1/s, respectively). Gray arrows indicate high exhumation rates (>8 mm/year, see Figure 6). Proshear and retroshear zones are labeled by "**p**" and "**r**," and crustal- and lithospheric-scale shear zones by "**C**" and "**L**." The results of the presented experiments are symmetrical with respect to the central vertical cross section A1-A2.

2.2. Modeling Procedure and Free Parameters

In total, we performed 15 different experiments by varying three controlling parameters (Table 1): (1) rheological structure of the overriding continental lithosphere, (2) contribution of upper plate advance (V_{Adv}) in the total shortening rate (V_{Tot}), and (3) width of the indenter in the x direction.

We compare our simulations with three reference experiments (models **1–3**; Figures 3–6 and S1–S3 and Table 1) characterized by different rheological profiles (Figure 2b1) ranging from strongly coupled (model **1**) to weakly coupled (model **3**) and including an intermediate case (model **2**). The degree of mechanical coupling of the overriding plate is controlled by the lithology of the lower crust and by the initial crustal
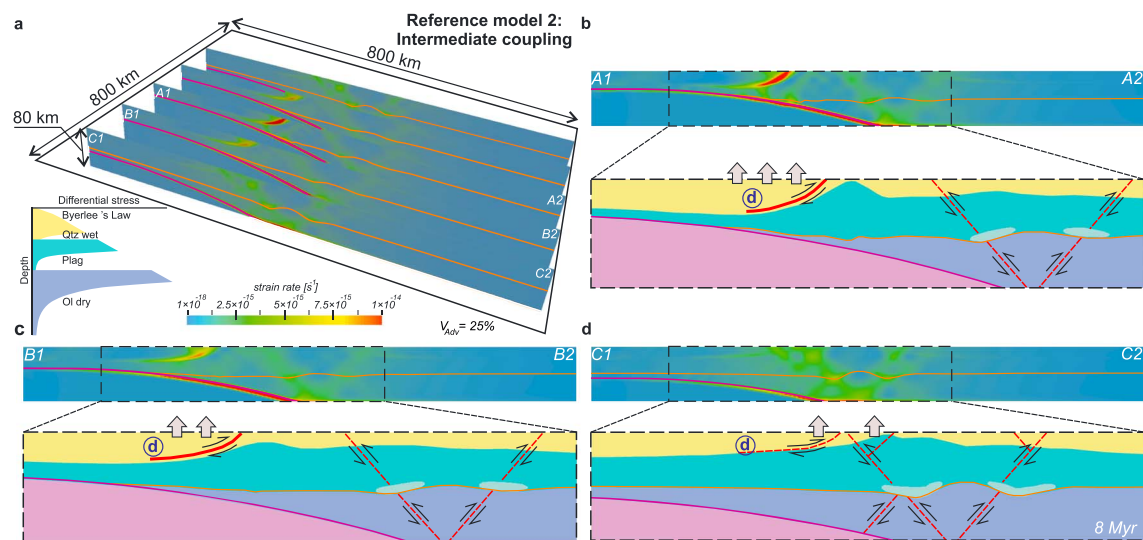

Figure 4. Reference experiment for intermediate rheological coupling of the overriding lithosphere (model **2**) after 8-Myr modeling time. Light aqua areas refer to distributed (nonlocalized) ductile strain in the lowermost crust. Deformation localizes along both the shallowly dipping (≤30°) retrodecollement (labeled by "**d**") and steeply dipping (~60°) shear zones.
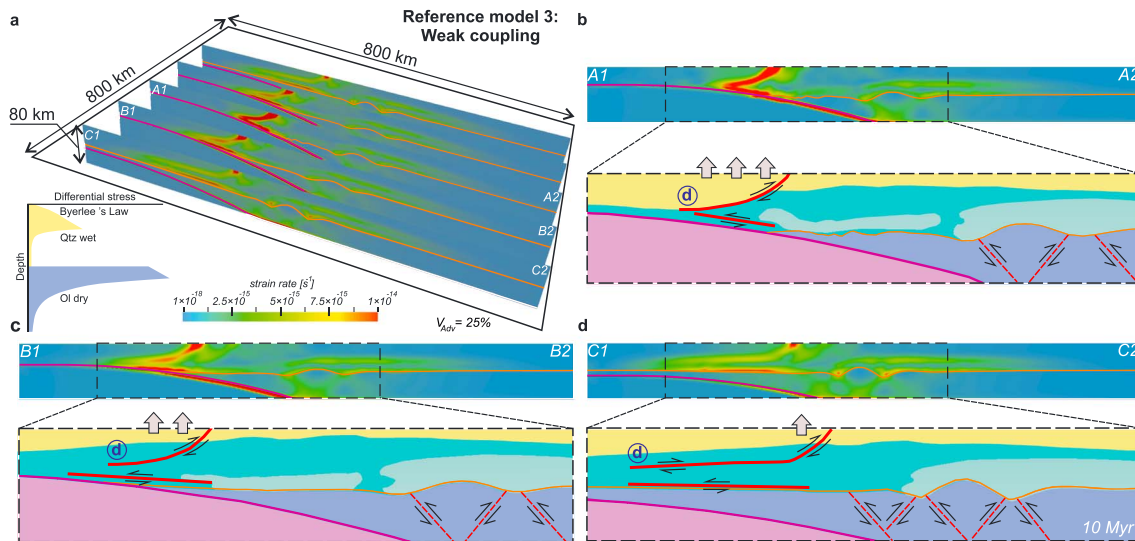
Figure 5. Reference experiment for weak rheological coupling of the overriding lithosphere (model **3**) after 10-Myr modeling time. Most of deformation concentrates in the shallow retrodipping decollement (labeled by "**d**") rooting into an underlying ductile lower crust.

geotherm. The mafic lower crustal composition (corresponding to the dry diabase flow law) combined with a relatively "cold" geotherm (465 °C at the Moho, resulting from no crustal heat production) leads to a very thick brittle part of the lower crust that almost completely couples the strain of the upper crust and lithospheric mantle (strong rheological coupling; model **1**). In contrast, a felsic lower crust (wet granite flow law) and "normal" crustal geotherm (610 °C at the Moho due to radiogenic heat generation in the crust) results in a completely ductile lower crust playing the role of a weak layer that decouples the brittle uppermost mantle and upper crust (weak rheological coupling; model **3**). The combination of a mafic lower crust and "normal" geotherm corresponds to the intermediate case (intermediate rheological coupling; model **2**) where the lower crust contains a brittle layer (in contrast to weakly coupled model **3**), which is thinner compared to model **1**. In all reference experiments (models **1**–**3**), we use following values for two remaining controlling parameters: 25% of upper plate advance (i.e., V_{Sub} = 22.5 mm/year and V_{Adv} = 7.5 mm/year) and a 300-km indenter width (see Figure 2b).

In the case of a weakly coupled upper plate (see Table 1), we tested the impact of the partitioning of velocity boundary conditions (models **4**–**6**; Figures 7 and S4–S7): V_{Adv} varied from 0% (V_{Sub} = 30.0 mm/year and V_{Adv} = 0.0 mm/year) to 50% (V_{Sub} = 15.0 mm/year and V_{Adv} = 15.0 mm/year) and also to 100% (V_{Sub} = 0.0 mm/year and V_{Adv} = 30.0 mm/year). Furthermore, we used different widths of the flexural bulge (Figures 8 and S8) for all coupling cases, including narrower (150 km wide, models **7**–**9**) and a wider indenter (450 km wide, model **10**). Finally, we investigate the effect of a narrow indenter width (150 km) combined with different values for upper plate advance (0%, 50%, and 100%) in models **11**–**13** (Figure 9), as well as different degrees of coupling under no upper plate advance (V_{Adv} = 0%) in models **14**–**15** (Figure S11).

3. Results

3.1. Effect of Rheological Structure of the Overriding Continental Lithosphere: Reference Experiments (Models 1–3)

3.1.1. Strong Rheological Coupling (Model 1)

The first reference experiment (model **1**; Figures 3, 6a, and S1) is characterized by strong rheological coupling of the overriding plate and by the reference boundary velocities (25% of upper plate advance) and indenter configuration (300 km wide in *x* direction).

A vertical cross section in the *y* direction through the segment corresponding to a background subducting plate (i.e., nonindenter portion outside of the central bulge; section C1-C2 shown on Figure 3d) indicates two oppositely dipping thrust-sense shear zones (localized strain rate >8 × 10^{-15} 1/s) rooting at an angle of ~60° next to the intersection of the subducting plate at the bottom of the model domain, referred to
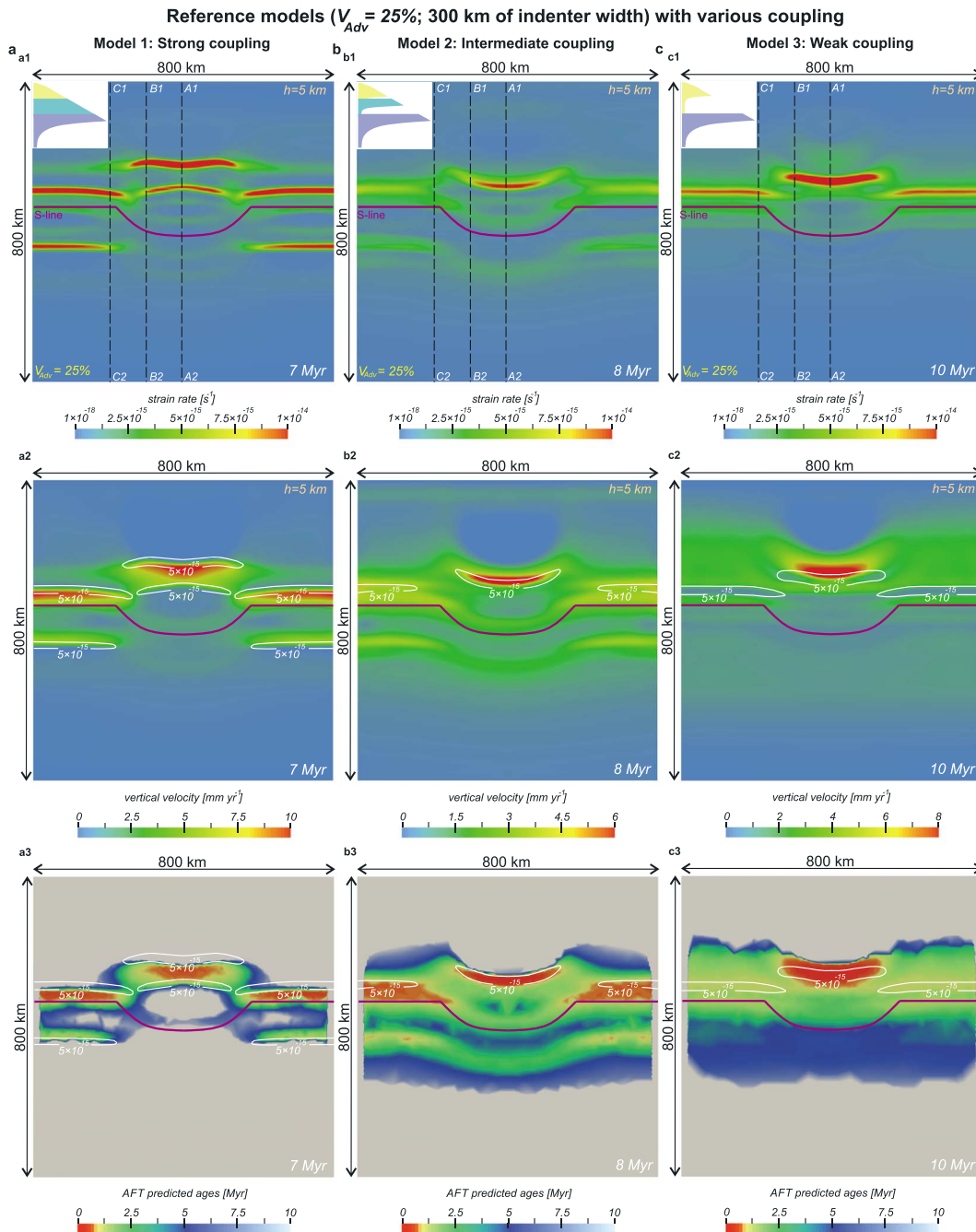
Figure 6. Plan views showing second invariant of computed strain rate and modeled vertical velocity (both at the 5-km depth; top and middle row, respectively) as well as predicted apatite fission track (AFT) ages (at the surface; bottom row) for the reference experiments characterized by different degrees of upper plate mechanical coupling: (a) strong coupling (model **1**), (b) intermediate coupling (model **2**), and (c) weak coupling (model **3**). White isolines in the middle and bottom rows outline the areas of the highest strain rate ($>5 \times 10^{-15}$ 1/s, see top row). Dashed lines indicate locations of the vertical cross sections shown on Figures 3–5. The weak rheological coupling (c) favors an isolated high (>8 mm/year) rock uplift developed over the central convex-upward indenter without any particular localization above background down-going plate.

here as the S line (see Figure 2). Two additional V-shaped wedges originate at these proshear and retroshear bands at the vertical level close to the Moho (Figures 3d and S1c, profile B1-B2). These shear bands create pop-up structures that are characterized by strong upward deflection of the upper-lower crust boundary (see interpretation profile on Figure 3d) and corresponding localized surface uplift (gray arrows on Figure 3d) in two narrow bands parallel to the plate interface (see plan view of rock uplift rate on Figure 6, slice
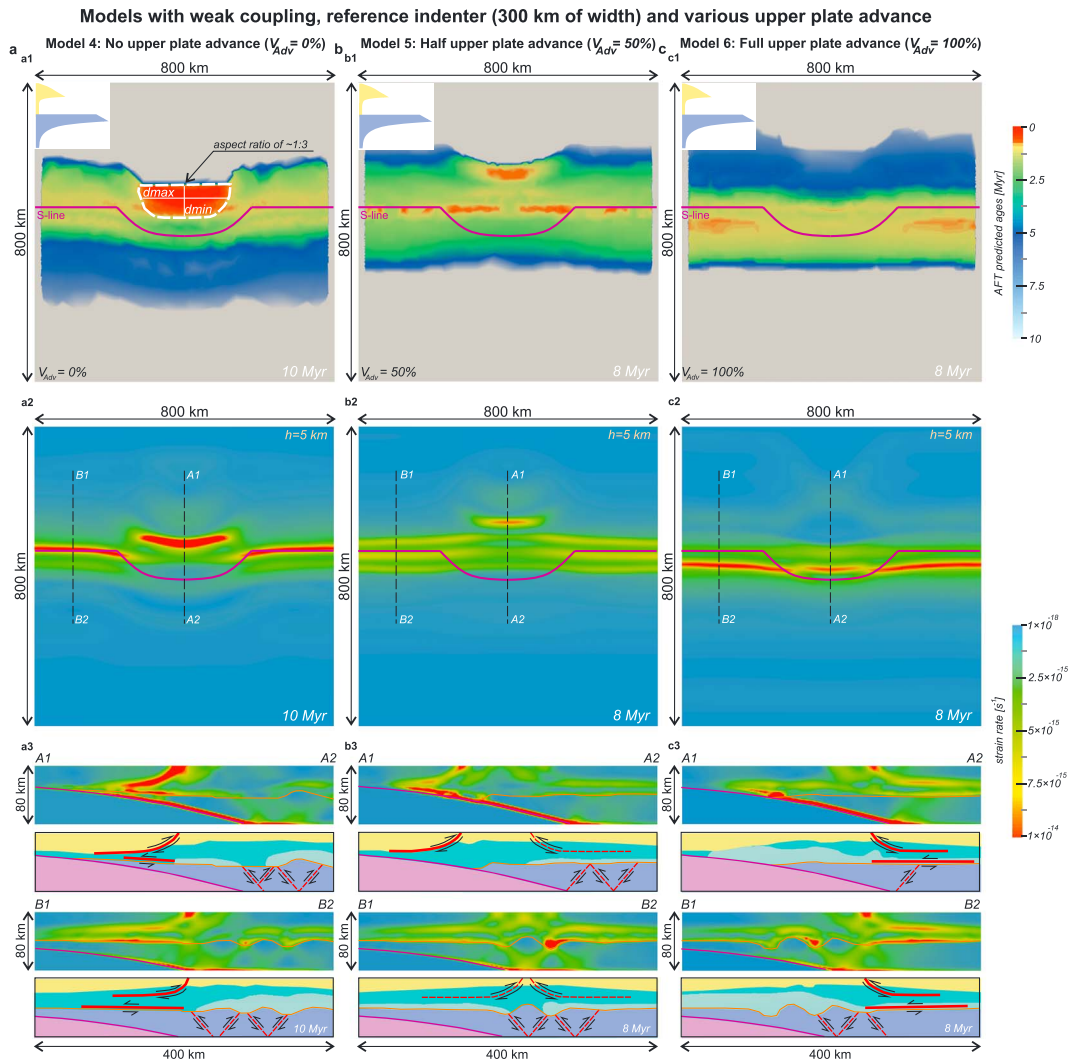
Figure 7. Plan views showing predicted apatite fission track (AFT) ages (top row) and strain rate (middle row), and corresponding vertical cross sections (bottom third) for the experiments characterized by weak rheological coupling of the overriding plate, reference indenter width (300 km) and different velocity boundary conditions: (a) no upper plate advance model **4** ($V_{Adv} = 0\%$), (b) half upper plate advance model **5** ($V_{Adv} = 50\%$), and (c) full upper plate advance model **6** ($V_{Adv} = 100\%$). White dashed line on a1 indicates ellipsoidal zone above the indenter apex characterized by the youngest predicted (<1 Myr) AFT ages corresponding to localized rapid rock exhumation. Maximum and minimum diameter of this area are labeled by "dmax" and "dmin"; their relation defines the aspect ratio (1:3 in this case) for the corresponding curved ellipse region (see also Figures 8 and 9).

a2, and predicted AFT ages on Figure 6, slice a3). Along the entire length of the background slab segments (i.e., outside of the central part of the model), both deformation and associated rock uplift are better localized on the proside, while the retroside expression is weaker but still clearly visible in both the second invariant of strain rate tensor and vertical velocity fields (see Figures 3d and 6a).

These lithospheric-scale shear bands (i.e., shear bands cutting the entire model domain from the crust to the lithospheric mantle), however, attenuate toward the indenter in the model center, where deformation is accommodated along two different shear zones that nucleate where the subducting plate interface intersects the overriding plate's Moho (Figures 3b and 3c). As shown in plan view (Figure 6, slice a1), these crustal-scale shear zones (i.e., shear zones limited to the upper and lower crust) are shifted toward the down-going plate where they form an undeformed yet uplifted V-shape wedge directly above the indenter apex. Note that attenuated prolongation of proside shear zone of this wedge into adjacent areas of background slab (Figure 6, slice a1) can also be distinguished on corresponding vertical profiles (Figures 3d and S1c, profile B1-B2) as an additional proshear zone outboard of the principal wedge developed between the lithospheric-scale shear bands.
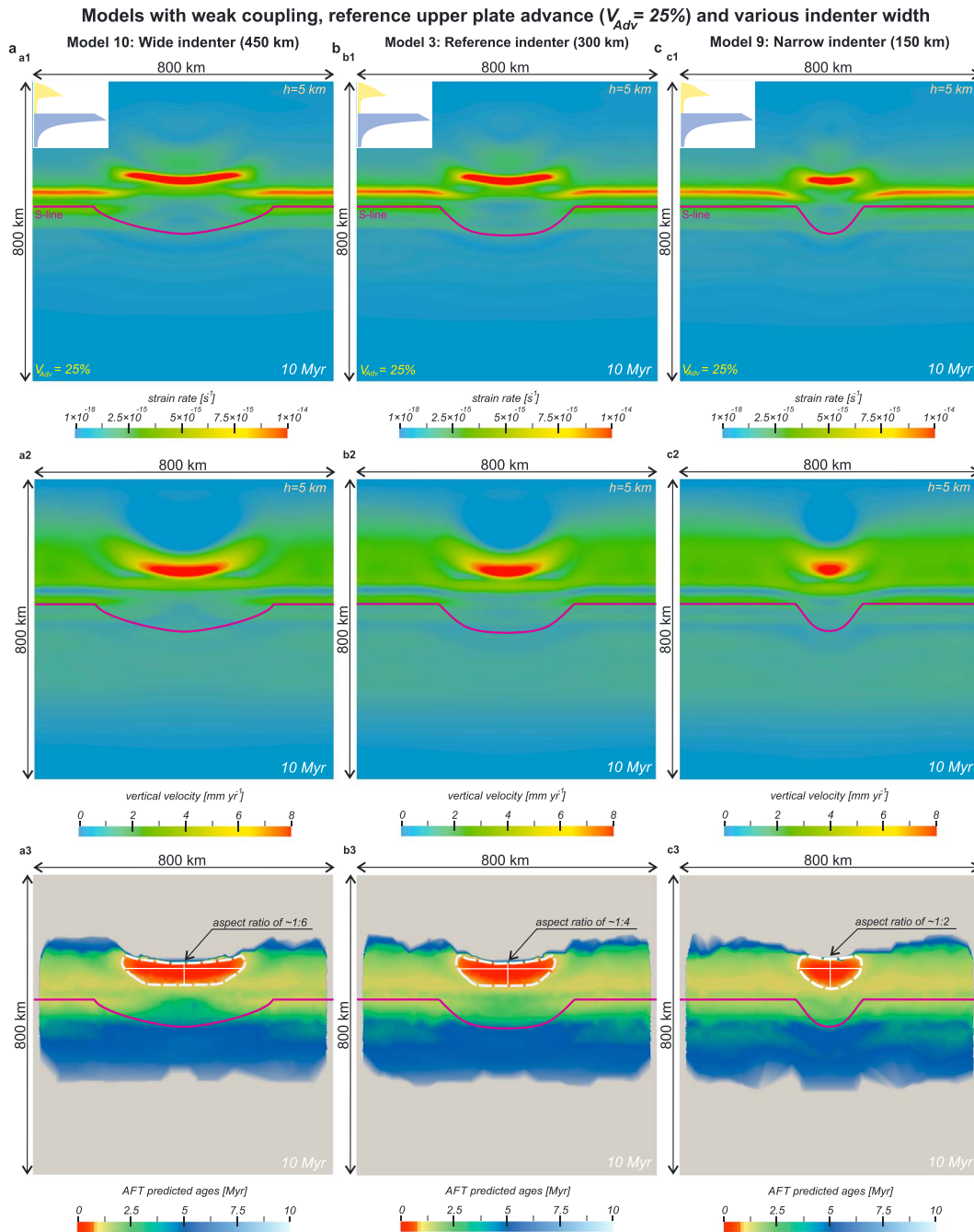
Figure 8. Experiments characterized by weak rheological coupling of overriding plate, reference upper plate advance (V_{Adv} = 25%) and different indenter width: (a) wide indenter model **10** (width of 450 km), (b) reference indenter model **3** (width of 300 km), and (c) narrow indenter model **9** (width of 150 km). Indenter configuration controls a final shape of curved ellipse that bounds area of the youngest (<1 Myr) apatite fission track (AFT) ages.

To summarize, the essential feature of this strongly coupled reference experiment (model **1**) is that uplift is localized within small wedges confined between oppositely dipping shear zones (Figures 3b–3d). This is also reflected at the surface in the narrow (~50–75 km wide) bands of the highest vertical velocities (>8 mm/year) and associated youngest predicted (<1 Myr) AFT ages elongated in the trench-parallel direction (Figure 6, slices a2 and a3). Conforming to the different shear zones, this band is shifted by ~100 km toward the subducting plate above the indenter with respect to adjacent model segments.
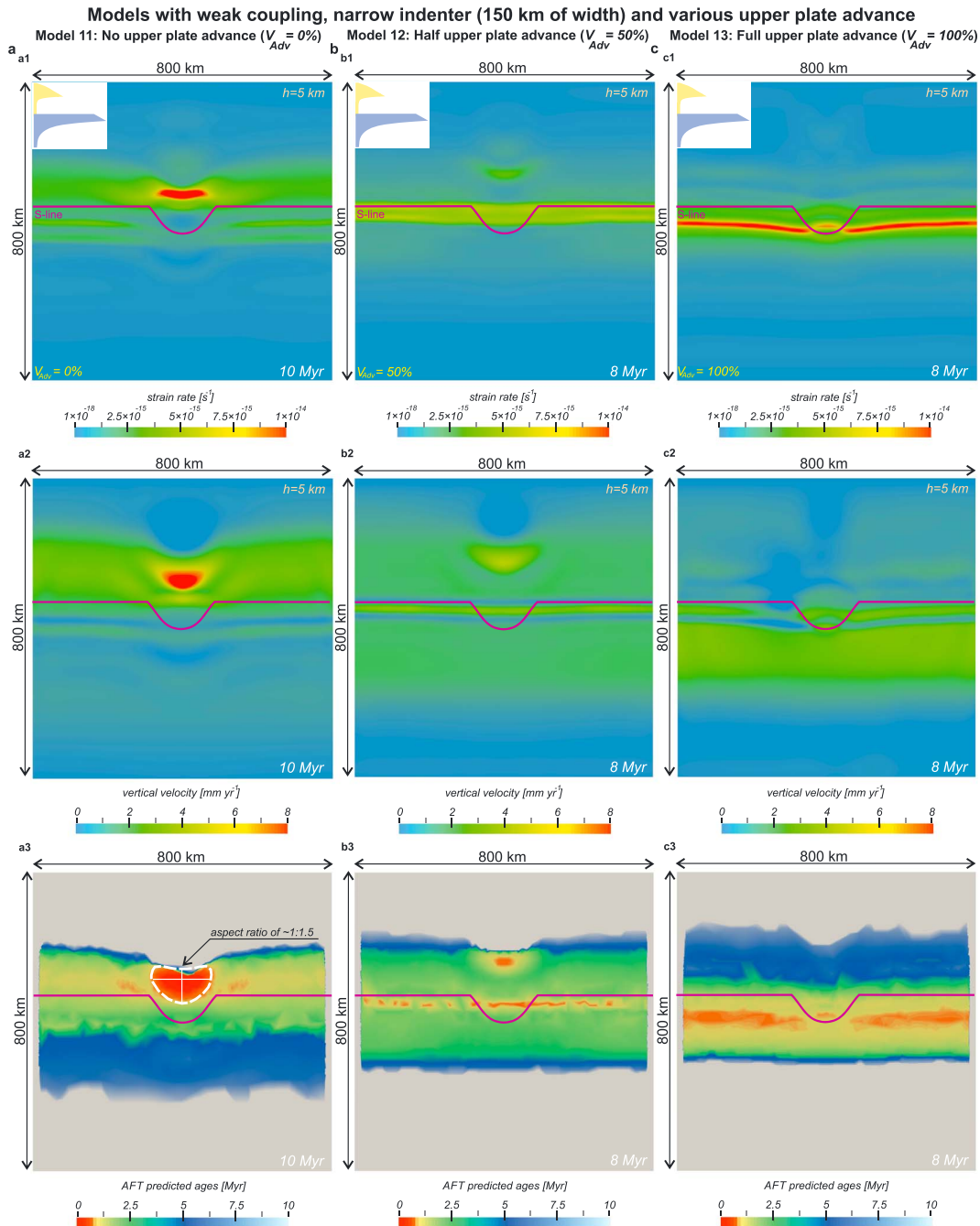
Figure 9. Experiments characterized by weak coupling of upper plate, narrow (150-km-wide) indenter and different velocity boundary conditions: (a) no upper plate advance model **11** ($V_{Adv} = 0\%$), (b) half upper plate advance model **12** ($V_{Adv} = 50\%$), and (c) full upper plate advance model **13** ($V_{Adv} = 100\%$). No upper plate advance contribution ($V_{Adv} = 0\%$) in the total shortening leads to an quasi-isometric (aspect ratio of 1:1.5) zone of localized exhumation above the indenter apex. AFT = apatite fission track.

3.1.2. Intermediate Rheological Coupling (Model 2)

The second reference experiment with intermediate mechanical coupling in the upper plate (model **2**; Figures 4, 6b, and S2) also includes steeply dipping shear zones crossing almost through the entire model domain and rooting into the S line at an angle of ~60°. However, compared to the previous strongly coupled model **1**, zones of elevated strain rate ($3-6 \times 10^{-15}$ 1/s) corresponding to these proshear and retroshear are much broader (tens of kilometers instead of some kilometers). In particular, due to the dominance of the ductile mode of deformation in the lowermost crust, relatively high strain rate intensity in this part of the

section could be interpreted as distributed ductile strain rather than as a fragment of continuous steep shear zone crossing through the Moho (see interpretation sections on Figures 4b–4d).

In contrast to the previous experiment (model **1**), most of the deformation here in model **2** is accommodated by a thin low-angle decollement dipping ≤30°. Localized strain rates reach their highest values (>8×10^{-15} 1/s) in the decollement above the indenter (Figure 4b). Toward the background subduction zones, this shallowly dipping structure attenuates (to ~$5–7 \times 10^{-15}$ 1/s) but remains discernible both in plan view and corresponding vertical cross sections (see Figure 6, slice b1, and Figure 4d, and Figure S2c, profile B1-B2, respectively).

In the hanging wall above the background slab, elevated values (>4.5 mm/year) of the rock uplift rate and associated young (<1 Myr) AFT ages are distributed along relatively wide (~150 km) bands parallel to the S line. However, the highest rock uplift rates (>5 mm/year) are concentrated within a narrow zone in the center of the model directly above the indenter (Figure 6, slice b2). Thus, even a small amount of rheological decoupling in the overriding plate (as adopted in model **2**) leads to a large change in the mode of localized uplift such that vertical movements occur in the hanging wall of the shallowly dipping decollements (Figures 4b–4d). This is in contrast to V-shaped wedges localizing vertical motion between steep fault zones that occur in the previous case of a strongly coupled lithosphere (model **1**; Figures 3b–3d).

3.1.3. Weak Rheological Coupling (Model 3)

The response of a weakly coupled overriding continent (model **3**; Figures 5, 6c, and S3) to subduction of the down-going rigid plate is the formation of a basal decollement dipping in retrodirection and rooting into an underlying ductile lower crust. In contrast to the previous models **1** and **2**, steeply dipping shear zones are confined to the deepest part of the model box (40- to 80-km depth) corresponding to the mantle part of the lithosphere and do not penetrate into the crust (see vertical sections on Figures 5b–5d). The lower crust is subjected to distributed ductile deformation with strain rates typical for broad shear bands in the previous models **1** and **2** ($3–6 \times 10^{-15}$ 1/s). Nevertheless, the rate of deformation can exceed 8×10^{-15} 1/s in several strongly localized Moho-parallel shear zones located in the lowermost part of the crust (Figures 5b–5d). Similar to the previous experiments (models **1** and **2**), the area of high localized strain rate (>8×10^{-15} 1/s) in the model center (above the indenter) is laterally shifted toward the subducting slab (see plan view in Figure 6c1).

The key feature of this weakly coupled reference experiment (model **3**) is that the highest near-surface rock uplift rates (>8 mm/year; Figure 6, slice c2) and corresponding youngest AFT ages (<1 Myr; Figure 6, slice c3) are concentrated in a single elliptical area above the indenter apex. This result is in contrast to the previous models with strong (model **1**) and intermediate (model **2**) upper plate coupling where high vertical velocities and associated young thermochronometric ages localize not only above indenter but also above the background slab (Figures 6a and 6b).

3.1.4. Temporal Evolution of Reference Models 1–3

The rheological structure of the overriding lithosphere appears to be important not only in terms of the resulting deformation/rock uplift patterns of the reference models **1**–**3** (Figures 3–6) but also for their temporal evolution (Figures S1–S3). In the case of the intermediately coupled experiment **2**, strongly localized deformation and high rock uplift rates arise soon after the start of model (4 Myr) in the area above the central indenter (Figure S2a). Further system development (6–8 Myr) results in the appearance of secondary, more broadly distributed zones of high strain rate and uplift localization located over background segments of the subducting slab (Figures S2b and S2c). In contrast, for the end-member cases of the lithospheric rheological structure (models **1** and **3**), initial strain localization along linear structures parallel to the plate margin and associated surface uplift first occur in the lateral ends of the orogen (at 3–5 Myr; see Figures S1a and S3a), whereas the indenter-centered zone of rapid deformation and large vertical velocities develops later, at the mature stage only (5–10 Myr; Figures S1b and S1c and Figures S3b and S3c). However, only the strongly coupled end-member (model **1**) results in the final coexistence of both central and peripheral localized rock exhumation (Figure 6, slices a2 and a3, and Figure S1, slice c1). In contrast, in the case of the weakly coupled experiment (model **3**), the rock uplift pattern evolves from linear trench-parallel bands over the areas distant from the indenter (Figure S3, slice a1) to an isolated curved ellipse in the hanging wall above shallow decollement in the center of the model (Figure 6, slices c2 and c3, and Figure S3, slice c1).

3.2. Effect of the Partitioning of Velocity Boundary Conditions (Models **4**–**6**)

Models **4**–**6** explore the relationship between boundary velocities applied at the left ($y = 0$ km; subduction and accretion) and right ($y = 800$ km; upper plate advance) sides of the model domain (see Figure 2) for the case of a weakly coupled overriding lithosphere (Table 1). Models **4** (Figure 7a), **5** (Figure 7b), and **6** (Figure 7c) correspond to 0%, 50%, and 100% of upper plate advance (velocity at the right side; V_{Adv}) in the total shortening ($V_{Tot} = 30$ mm/year), respectively.

The no upper plate advance experiment **4** ($V_{Adv} = 0$%; Figures 7a and S4a) produces a deformation and rock uplift pattern that is similar to that of the corresponding reference model **3** ($V_{Adv} = 25$%; Figure 6c). The main difference is the aspect ratio of the elliptical zone (ratio between its shortest and longest axes) of rapid uplift (>8 mm/year) and youngest (<1 Myr) AFT ages above the indenter increasing from ~1:4 to ~1:3 as upper plate advance decreases from 25% (model **3**; Figure 6, slice c3) to 0% (model **4**; Figure 7, slice a1). Another important aspect of this no upper plate advance case is that the shallowly dipping decollement developing at the initial stage of orogen evolution (5 Myr) is not confined to the background slab section (as in reference model **3**—see Figure S3a) but crosses the entire width of the model domain forming a continuous initial linear band slightly bent by the subducting plate (Figure S5a).

Increasing the rate of upper plate advance to 50% (half upper plate advance case of model **5**; Figures 7b and S4b) leads to a significantly different system behavior: The localized uplift centered above the indenter becomes several times smaller in area, whereas another well-defined yet very narrow (<50 km) zone of young (<1 Myr) AFT ages spans the width of the model in the trench-parallel direction (Figure 7, slice b1). The central decollement dipping in the retrodirection (see vertical profile A1-A2 on Figure 7b) is less pronounced (localized strain rates of ~7–8 × 10^{-15} 1/s) compared to the no upper plate advance case (model **4**; Figure 7a, profile A1-A2). Here compressional deformation is additionally accumulated along a complementary broad shear zone located toward the continent and dipping in the opposite, prodirection. This second shallowly dipping zone of poorly localized strain (~4–7 × 10^{-15} 1/s) can be clearly identified on both central and peripheral cross sections (compare Figure 7b, profiles A1-A2 and B1-B2, respectively). The vertical section B1-B2 across the background subduction segment shows an almost symmetric deformation pattern with an identical degree of development in both the retrodecollement and prodecollement shear zones (Figure 7b, profile B1-B2) with positions remaining stable over the time scale considered (see Figure S6).

The shallow decollement zone dipping in the prodirection becomes the principal structure localizing crustal strain in the case of full upper plate advance model **6** ($V_{Adv} = 100$%; Figures 7c and S4c). In contrast to all previous experiments, no particular zone of indenter-related localized surface uplift can be observed in this model (Figure S4, slice c2). As a result, exhumation is poorly localized and AFT ages form a broad, straight band with only small variations between the indenter and background slab sections (Figure 7, slice c1). The temporal evolution of this experiment (see Figure S7) is characterized by a transition from slightly concave (Figure S7a) to quasi-linear (Figure S7c) shape of the localized near-surface deformation (in plan view) due to a slow lateral shift of the shallowly dipping shear zone accumulating most of the crustal deformation toward the right side of the model in the subduction peripheral segments (see vertical profile B1-B2 on Figure S7).

As shown by Nettesheim et al. (2018), increasing total convergence rate (V_{Tot}) up to 60 mm/year (instead of 30 mm/year) leads to higher maximum values of the vertical uplift (16 mm/year instead of 8 mm/year) without a change in the relative distribution of deformation and surface uplift. Therefore, the magnitude of total shortening plays a minor role in the resulting deformation and rock exhumation pattern in comparison to the relationship between boundary velocities applied at the opposite sides of the model.

3.3. Effect of Indenter Configuration (Models **7**–**15**)

We evaluate the effect of a narrower flexural bulge (150 km of the width in *x* direction instead of 300 km as adopted in previous experiments) and different degrees of upper plate rheological (de)coupling in models **7**–**9** (see Figure S8). In these, the upper plate advance contribution (V_{Adv}) in the total shortening (V_{Tot}) corresponds to a reference value of 25%.

Strongly and intermediately coupled experiments (models **7** and **8**, respectively) result in narrow (~100–150 km across) trench-parallel bands of anomalously young (<1 Myr) AFT ages, which are thinner

(~75 km across, model **8**; Figure S8, slice b3) or interrupted (model **7**; Figure S8, slice a3) in the central part directly above the narrow indenter. In contrast to corresponding models with reference indenter widths of 300 km (models **1** and **2**), these narrow indenter experiments (models **7** and **8**) show no isolated areas of increased uplift but are rather characterized by a continuous straight line of rock exhumation, as indicated by thermochronological ages (compare Figures 6a and 6b and Figures S8a and S8b). This strongly reduced effect of a narrower indenter on upper plate deformation is in agreement with findings reported by Nettesheim et al. (2018) for half upper plate advance ($V_{Adv} = 50\%$) experiments.

In contrast, the weakly coupled narrow indenter experiment (model **9**; Figure 8c) reproduces all the key features typical for the corresponding reference model **3** with indenter width of 300 km (Figure 6c). The area of high vertical velocities (>8 mm/year) and young AFT ages (<1 Myr) in the center of the model remains in the same spatial location, and its elliptical shape becomes more isometric: The ellipse aspect ratio decreases from ~1:4 to ~1:2 with the indenter narrowing from 300 to 150 km (compare Figure 6, slice c3, and Figure 8, slice c3). Correspondingly, deformation and rock uplift patterns for a wider indenter (model **10**; 450 km, see Figure 8a) are elongated with an aspect ratio of ~1:6 for the central area of fast uplift. Figure 8 shows a comparison of all three investigated indenter widths.

The combined impact of a narrower indenter width (150 km) and different magnitudes of subduction (V_{Sub}) and upper plate advance (V_{Adv}) components is presented in models **11**–**13** (Figure 9). These simulations are characterized by weakly coupled rheological structure of the overriding plate. As in the experiments with a reference indenter width (models **5** and **6** presented in section 3.2, see Figures 7b and 7c and Figures S4b and S4c), high upper plate advance ($V_{Adv} = 50\%$ and 100%; models **12** and **13**, respectively) does not lend to localized uplift above the indenter (Figures 9b and 9c). Accordingly, a decrease in the upper plate advance from values of the reference case ($V_{Adv} = 25\%$) to 0 ($V_{Adv} = 0\%$) contributes to a more isometric configuration of the uplift area (compare models **3** and **4** with $V_{Adv} = 25\%$ and $V_{Adv} = 0\%$ shown in Figures 6c and 7a, respectively). In model **11** (Figure 9a), we combine the narrowing effects of both the reduced upper plate advance component ($V_{Adv} = 0\%$) and narrower indenter shape (150-km width) that result in an almost circular rock exhumation pattern (ellipse aspect ratio ~1:1.5) that is in agreement with the localized bull's-eye surface deformation reported in syntaxial orogens (see Bendick & Ehlers, 2014, and references herein). This isolated indenter-centered area of anomalously high rock uplift rates (>8 mm/year) persists up to the depth of 15–20 km (Figure S9), whereas the corresponding thermal anomaly is shallower and completely disappears by 10-km depth (Figure S10).

Models **14** and **15** (Figures S11a and S11b) complete the comparison of the narrow indenter geometry by investigating upper plate rheology effects under no upper plate advance ($V_{Adv} = 0\%$) conditions. This series of models **14**, **15**, and **11** is analogous to the comparison of models **7**–**9** (with reference upper plate advance of $V_{Adv} = 25\%$) shown in Figure S8 with strong, intermediate, and weak coupling, respectively, and results in a similar trend (Figure S11). For intermediate or strong coupling (models **14** and **15**) rock exhumation evolves into continuous, linear zones elongated parallel to the trench. No localized exhumation over the indenter apex can be seen, this remains a feature solely found in case of a weakly coupled lithosphere (model **11**; Figures 9a and S11c).

4. Discussion

4.1. Summary of Numerical Results

Variations in the rheological coupling of the overriding continental plate lead to different structural styles of deformation. These styles range from steeply dipping shear zones cutting the entire model domain from the upper crust down to the lithospheric upper mantle (strongly coupled model **1**; Figure 3) to thin shallow decollements dipping in the retrodirection (weakly coupled model **3**; Figure 5). The intermediate case combines both of these two major types of localized deformation (intermediately coupled model **2**; Figure 4).

The common point of all reference experiments (models **1**–**3**) refers to the elongated areas of strong strain localization and associated focused rock uplift situated directly above the indenter apex (Figure 6). However, only the strongly coupled (model **1**) and weakly coupled (model **3**) end-member cases include well-developed faulting (localized strain rate of $>8 \times 10^{-15}$ 1/s) above the background subducting plate, whereas the intermediate model **2** shows an attenuated rate of deformation (~5–7 × 10^{-15} 1/s) outboard

of the indenter (compare Figure 6, slice a1; Figure 6, slice c1; and Figure 6, slice b1). The relatively weak and broad strain rate localization at the peripheral segments of the intermediately coupled lithosphere (model **2**) stem from the distribution of strain between both shallowly dipping decollements and steep shear zones (see corresponding vertical cross sections on Figures 4d and S2c, profile B1-B2). Nevertheless, localized fast rock uplift associated with these two structures (see gray arrows on Figure 4d) occurs in well-defined yet relatively wide (~150 km) trench-parallel bands in both the near-surface vertical velocities (>4.5 mm/year; Figure 6, slice b2) and predicted AFT ages (<1 Myr; Figure 6, slice b3). In contrast, the model with a weakly coupled rheological structure (model **3**; Figure 6, slice c1) develops a well-established decollement (localized strain rate of $>8 \times 10^{-15}$ 1/s) above the background slab sections, but no associated localized rock uplift (Figure 6, slice c2) or concentrated young AFT ages (Figure 6, slice c3) can be observed there. This feature distinguishes the weak rheological coupling in the overlying continent (model **3**; Figure 6c), which is the only of the three tested configurations that favors an isolated region of high vertical rock uplift rates (>8 mm/year) over the central convex-upward-shaped bulge without any particular localization above the background down-going plate.

For this weakly coupled lithosphere, additional parameters were investigated. Increasing the component of upper plate advance from reference value of $V_{Adv} = 25\%$ (model **3**; Figure 6c) to $V_{Adv} = 50\%$ (model **5**; Figure 7b) and $V_{Adv} = 100\%$ (model **6**; Figure 7c) disfavors localized surface uplift over the flexural bulge. On the contrary, no upper plate advance ($V_{Adv} = 0\%$, model **4** in Figure 7a) leads to a more symmetric shape of the indenter-centered ellipsoidal zone of high exhumation rates (ellipse aspect ratio increases from 1:4 to 1:3 with decreasing upper plate advance V_{Adv} from 25% to 0%; see Table 1). Additionally, the final configuration of the region of rapid exhumation is directly controlled by the shape of the indenter. Figure 8 compares results for deformation and rock uplift patterns for wide (450 km; model **10**), reference (300 km; model **3**), and narrow (150 km; model **9**) indenter widths. A wide indenter (450 km; Figure 8a) results in an elongated center of uplift with an aspect ratio of ~1:6, while narrowing of the indenter to 300 km width (Figure 8b) and to 150-km width (Figure 8c) leads to narrower ellipses with aspect ratios of ~1:4 and ~1:2, respectively. The combined effect of a narrow indenter (150-km width), shortening accommodated by subduction and accretion only (no upper plate advance; $V_{Adv} = 0\%$), and a weakly coupled lithosphere (model **11**, see Figure 9a) gives rise to a quasi-isometric (ellipse aspect ratio ~1:1.5) indenter-centered area of rock exhumation similar to the bull's-eye pattern observed in some syntaxial orogens (Bendick & Ehlers, 2014).

It is also worth noting that regardless of indenter width and the contribution of upper plate advance to total shortening, all experiments with a strongly (models **1**, **7**, and **14**) and intermediately (models **2**, **8**, and **15**) coupled overriding plate do not show a spatially localized bull's-eye-like rock uplift above the flexural bulge (see Figures 6, S8, and S11).

4.2. Conditions for Producing a Symmetric Zone of Rapid Exhumation

Based on the results presented, we find that a bull's-eye-like exhumation pattern characterized by a quasi-symmetric (aspect ratio close to ~1:1.5) shape of localized uplift can be reproduced by subduction of an indenter-shaped plate only with an appropriate combination of all three controlling parameters: boundary velocities (amount of upper plate advance), width of the flexural bulge, and rheological structure of the overriding continent (see "best fit" model **11** shown on Figures 9a and 10a).

In more detail, the relationship between subduction and upper plate advance components of the total shortening may control the resulting shape of the ellipse outlining the boundary of rapid uplift: Increasing the upper plate advance fraction from 0% to 25% leads to a small elongation of the ellipse and a decrease in the ellipse aspect ratio (from ~1:1.5 to ~1:2 in the case of the models with a relatively narrow indenter width of 150 km—see Figures 9a and 8c, respectively). On the other hand, an increase in upper plate advance to 50–100% leads to the development of decollements dipping in the opposite direction that prevent localization of indenter-centered rock uplift (Figures 7b and 7c). These tendencies persist for the models with various indenter configurations (from 300 to 150 km wide; see Figures 7 and 9, respectively, and Table 1).

Second, the initial shape of the indenter plays an important role as well since even under the appropriate boundary conditions (upper plate advance of 25%) a wider indenter (450 km width) provides a considerably elongated zone of localized uplift (aspect ratio of ~1:6) that is too asymmetric to be classified as a bull's-eye structure (Figure 8a).
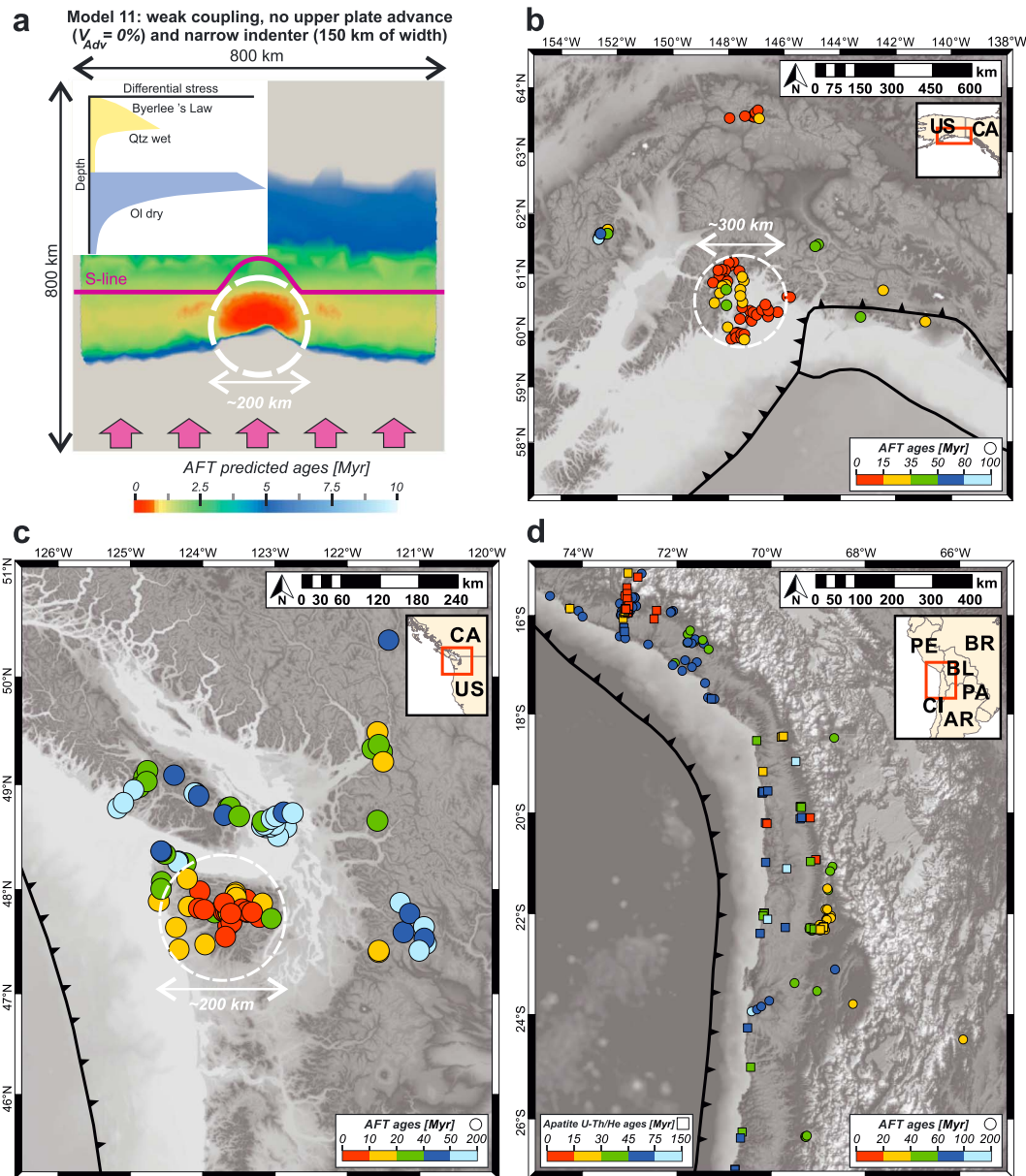
Figure 10. Comparison between modeled and observed spatial distributions of thermochronological cooling ages. (a) Predicted apatite fission track (AFT) ages for model **11** characterized by weakly coupled rheological structure and no upper plate advance contribution ($V_{Adv} = 0\%$) in the total shortening and relatively narrow indenter width (150 km). (b–d) measured thermochronological cooling ages: (b) the Southeast Alaska (Arkle et al., 2013; Benowitz et al., 2011, 2012; Ferguson et al., 2015; Haeussler et al., 2008; O'Sullivan et al., 1997; Plafker et al., 1989; Spotila et al., 2004); (c) the Olympic Mountains of the Cascadia subduction zone (Brandon et al., 1998; Currie & Grist, 1996; England et al., 1997; Johnson et al., 1986; Reiners et al., 2002); and (d) the South American subduction zone (Andriessen & Reutter, 1994; Avdievitch et al., 2018; Barnes et al., 2008; Gunnell et al., 2010; Juez-Larré et al., 2010; Maksaev & Zentilli, 1999; McInnes et al., 1999; Noury et al., 2016; Schildgen et al., 2007, 2009; Wipf, 2006; Wipf et al., 2008). White circles indicate the concentric zones of vertical advection (bull's-eye pattern) in the modeled (a) and observed (b, c) AFT ages fields. No localized bull's-eye pattern characteristics associated with focused exhumation are detected in the overriding plate of the South American subduction zone (d).

Finally, we find that the rheological structure of the overlying lithosphere appears to be the most important controlling parameter for the localization of deformation. Strong-to-intermediate mechanical coupling between the upper crust and lithospheric mantle is incompatible with an axisymmetric bull's-eye exhumation pattern (Figures 3, 4 and 6a and 6b), even in the case of a considerably narrower indenter (Figures S8a and S8b) and no upper plate advance (Figures S11a and S11b). In contrast, a weakly coupled rheological profile isolates and concentrates rock uplift within a single indenter-centered zone (Figure 6c). Its geometry is further modified by the contribution of upper plate advance in the total shortening (Figure 7a), the indenter

shape (Figure 8c), or both of them (Figure 9a). This is in agreement with a worldwide estimate of the lithospheric strength envelope showing that the upper continental crust is, in general, mechanically decoupled from the mantle within active subduction and collision zones (see Figure 4a in Tesauro et al., 2012).

To summarize, the subduction of a flexural bulge is a necessary but insufficient condition for spatial localization of anomalous exhumation rates within isometric (~1:1.5 aspect ratio) and small (~100-km diameter) bull's-eye regions. We suggest that other appropriate initial and boundary conditions including mechanical decoupling in the overriding lithosphere, relatively narrow indenter, and the dominance of subduction shortening are also required.

4.3. Rheology and Structure of the Continental Lithosphere in Orogen Syntaxes

As shown above, rheological properties of the overriding continental lithosphere may be a crucial parameter for the resulting deformation pattern in orogen syntaxes since even relatively small variations in mechanical coupling of the upper crust and lithospheric mantle cause large changes in the way upper plates strain is localized. The transition from strongly to intermediately/weakly coupled lithosphere switches the deformation mode from steep dipping shear zones that penetrate the entire model domain to shallowly dipping decollements rooting into the ductile lower part of the crust. The latter appears to be favorable for localized uplift above an indenter with concentrated vertical movements in the hanging wall. This uplift could be expressed at the surface through a characteristic bull's-eye structure under conditions of not only an appropriate degree of decoupling but also from a relatively narrow indenter configuration and small fractions (<25%) of upper plate advance. Despite the importance of the indenter geometry and velocity boundary conditions, our models identify a rheologically decoupled overlying lithosphere to be the key causal factor for spatially focused, rapid exhumation as it is observed in many transition zones of syntaxial orogens.

The long-term strength of lithosphere described by the Brace-Goetze yield-stress envelopes (Brace & Kohlstedt, 1980; Goetze & Evans, 1979) varies as a function of depth according to the plastic (e.g., Mohr-Coulomb failure criterion) and viscous (e.g., power law dislocation creep) deformation laws (see the numerical methods section in supporting information). The continental crust can provide a very large variety of possible rheological profiles due to variations in its structure and composition (Figure 2b) compared to oceanic crust. Considerable contrasts in rheological strength profiles between different segments of the continental part of the lithosphere have been reported by both geological observation and theoretical studies (see Burov, 2011, and references therein). The principal reason for this high diversity resides in the ductile parts of the crust, which are strongly influenced by the crustal thermal structure. That, in turn, is usually not well constrained because of the high uncertainty in (1) a region's thermal history (continents may have undergone several major thermal events), (2) current thermal thickness of the continents (defined by the depth of the 1330 °C isotherm), and (3) the distribution of radiogenic heat production in the crust that can contribute up to 50% of the continental surface heat flux. Moreover, unlike largely rock-independent brittle strength (Brace & Kohlstedt, 1980; Byerlee, 1978; Kohlstedt et al., 1995; Yamato & Brun, 2017), viscous parameters are also conditioned by rock type that may refer to either "strong" (wet granite flow law) or "weak" (dry diabase flow law) lower crust (Carter & Tsenn, 1987; Ranalli, 1995)—see supporting information Table 1. As shown in a review by Burov (2011), rheological decoupling should always occur in felsic-dominated crust (except for extremely thin, <20 km, rifted crust). In contrast, other crustal compositions (including a mafic lower crust) might result in strongly coupled lithosphere but only if the thermotectonic age is very old (>750 Myr). This means that a certain degree of the mechanical decoupling between the crust and lithosphere is the typical case of the rheological structure of continents except for old cratonic regions and thus can be applied for a broad range of possible geodynamical settings around the world. According to the global map of lithospheric strength (Tesauro et al., 2012), the lowest values of the integrated strength of the continental lithosphere (<2.0 × 10^{13} Pa·m) and associated decoupled rheological structure are mostly found in collisional belts and subduction zones. This ties into the principal findings of our study showing that bull's-eye rock exhumation at orogen syntaxes can be developed only in a weak, decoupled overriding plate.

Nevertheless, despite the progress in understanding the long-term strength of lithosphere (Burov, 2011; Tesauro et al., 2012, 2013), rheological parameters remain highly uncertain, and many additional sources of independent data are needed for further specification on the rheological profiles in different continental settings. They include seismic, petrologic, and gravitational data, as well as seismicity and surface heat flow distributions. Effective elastic thickness estimates provide a direct proxy for integrated strength of the

lithosphere (Burov & Diament, 1995). Results of numerical and analog modeling also represent an independent class of constraints on the choice of the crustal rheology, since they allow identification of the surface and subsurface deformation patterns formed in response to different rheological models. In particular, the numerical experiments presented in this study assess the effects of the rheological structure of the overriding plate on the deformation and surface uplift patterns in the context of the subduction of a flexural bulge.

4.4. Link to Previous Studies

In most previous numerical modeling studies, contractional stresses and deformation at convergent plate boundaries have been investigated through 2-D vertical sections (e.g., Billen, 2008; Burov & Yamato, 2008; Ficini et al., 2017; Gerya et al., 2004, 2008; Grove et al., 2009; Yang et al., 2018) or by global (e.g., Bird, 1998; Bird et al., 2008; Coblentz et al., 1994; Koptev & Ershov, 2010; Lithgow-Bertelloni & Guynn, 2004; Naliboff et al., 2012; Wu et al., 2008; Yang & Gurnis, 2016) and regional (e.g., Coblentz & Richardson, 1996; Liu & Bird, 2002a, 2002b; Rajabi et al., 2017; Richardson & Reding, 1991) spherical shell models. Less common in previous work are 3-D modeling studies, and their focus is on subduction initiation (Gerya et al., 2015; Stern & Gerya, 2018), subduction obliquity (Plunder et al., 2018), lateral transition from oceanic subduction to continental collision (Li et al., 2013; Menant et al., 2016; Moresi et al., 2014; Pusok et al., 2018; Pusok & Kaus, 2015; Sternai et al., 2014) and the related impact of slab detachment in orogenic belts (Capitanio & Replumaz, 2013; Replumaz et al., 2014; Duretz et al., 2014; see also analogue laboratory experiments by Faccenna et al., 2006), opposing continental subduction zones (Liao et al., 2017), or subduction of cylindrical plates (e.g., Koons et al., 2010; Schellart et al., 2007) without particular focus on the effects of the subducting plate's internal 3-D geometry.

In contrast, Bendick and Ehlers (2014) investigated the impact of subducting plate geometry on upper-plate deformation. They attributed rapid localized exhumation (a bull's-eye pattern of surface deformation) reported in many transition zones between adjacent plate boundary segments around the world (e.g., the Southeast Alaska and the Cascadia subduction zone—see, e.g., Enkelmann et al., 2017; Brandon et al., 1998) to convex-upward-shaped flexural bulges of the subducting plate. However, the models in Bendick and Ehlers (2014) employed a simplified purely viscous rheology, which excludes brittle strain localization that has been shown to be important for the deformation and topographic evolution of the orogens (see, e.g., Vogt et al., 2017, 2018).

In view of the recent conceptual and methodical advances in our understanding of the rheological stratification of the lithosphere (Burov, 2011, and references therein), Nettesheim et al. (2018) investigated the subduction of an indenter-shaped plate with a layered viscoplastic upper plate. These models provided the basis on which this study was designed. However, their study focused on the effects of velocity conditions and variations in erosional efficiency. It did not consider the degree rheological coupling between the upper and lower crust, the parameter we found to be of high importance but restricts itself to the configuration of our intermediately coupled models **2**, **8**, and **15**. Moreover, Nettesheim et al. (2018) did not reproduce the concentric bull's-eye-like (with a characteristic diameter of ~100+ km) rock uplift as observed in extreme syntaxial orogens (Bendick & Ehlers, 2014).

4.5. Model Limitations and Perspectives

The extremely high erosional efficiency adopted in this study has a twofold effect: On one hand, it leads to unloading the topographic stresses that amplifies strain localization (Roy et al., 2016) in shear zones and decollements. On the other hand, it promotes an overestimation of the rock uplift that becomes close to the rock exhumation under nearly total erosion (England & Molnar, 1990). As a result, the absolute values of predicted AFT ages (<1 Myr within bull's-eye structures) are younger compared to observed ones (Figure 10). Nevertheless, a modeled bull's-eye-like age pattern (Figure 10a) resembles the known isometric structures with a characteristic size of ~200 km as observed in the Southeast Alaska (Figure 10b) and the Olympic Mountains (Figure 10c). In contrast, despite thick and mechanically weak crust in the central Andes (Capitanio et al., 2011; Kley & Monaldi, 1998; Sobolev & Babeyko, 2005), no concentric uplift is reported in the South American subduction zone (Figure 10d), possibly because of a relatively small concavity of the subducting plate (see Figure 1d) and considerable upper plate advance component due to accelerated westward drift of the South American plate during the past 30 Myr (Russo & Silver, 1996; Silver et al., 1998) and finally perhaps due to the limited exhumation magnitudes in the region due to the arid to hyper

arid climate in the region. However, despite the lack of localized exhumation observed in the Arica bend of the central Andes due the arid climate, the long-wavelength topography of the region is highest at the Arica bend, before decreasing slightly to the south, away from the bend (Starke et al., 2017). This regional trend of decreasing elevations away from the Arica bend that is consistent with the high rock uplift rates predicted here above the bend causes higher elevations (in the absence of erosion).

Our generalized model setup does not aim to reproduce a specific region due to the restricted size of the model domain, the simplified erosional model, and the rigid slab rheology. However, this modeling approach can be used as an additional constraint for forthcoming geophysical studies because a comparison of the modeling results with observed structural features may help to discriminate the range of possible rheological (and thus compositional and thermal) characteristics that are permissible for a given geodynamic and geotectonic environment.

5. Summary and Conclusions

We presented results from numerical experiments that explore the three-dimensional response of a rheologically stratified overriding continental lithosphere to subduction of a rigid plate having a curved forward bulge. In this study, we have tested three controlling parameters (see Table 1): (1) rheological structure of the upper plate, (2) partitioning of velocity boundary conditions, and (3) indenter width. From this, we draw the following conclusions:

1. The rheological structure of the overriding plate plays a key role in the resulting deformation pattern: Strong rheological coupling favors steep dipping thrust-sense shear zones cutting the entire crust and the upper mantle; weakly coupled lithosphere, in contrast, localizes most of the deformation along shallowly dipping decollements rooting into ductile lower crust.
2. In the strongly coupled experiments, localized uplift within small V-shaped wedges squeezed between steep oppositely dipping shear zones is represented in plan view as narrow bands of rapid rock exhumation elongated perpendicular to the subduction direction and crossing through the entire model domain. In contrast, a rheologically decoupled lithosphere shows an isolated elliptical area of the highest rock uplift rates related to vertical movement in the hanging wall of the shallow retrodipping decollement developed in the continental crust over a central convex-upward-shaped indenter.
3. Increasing the component of upper plate advance in the shortening (i.e., the boundary velocity defining material influx in the direction opposite to that of the subduction of the down-going slab) disfavors localized surface uplift above an indenter. In contrast, shortening accommodated by subduction and accretion only (no upper plate advance case; $V_{\text{Adv}} = 0\%$) results in a more isometric geometry of the indenter-centered zone of high exhumation rates.
4. In the case of a weakly coupled continental lithosphere, the resulting aspect ratio of the elliptical zone of high uplift rate is conditioned by the indenter geometry. In particular, an extremely narrow indenter (150-km width) results in a considerably more isometric shape of the final ellipse compared to that of a reference (300-km width) and wide indenter (450-km width) experiments.
5. Experiments with an appropriate combination of the upper plate rheological structure (weakly coupled upper crust and lithospheric mantle), velocity boundary conditions (limited upper plate advance), and indenter shape (narrow width) excites a bull's-eye-like exhumation pattern that resembles the concentric structures of vertical advection observed at orogen syntaxes in such regions as the Southeast Alaska and the Cascadia subduction zone (western USA).

References

Andriessen, P. A., & Reutter, K. J. (1994). K-Ar and fission track mineral age determination of igneous rocks related to multiple magmatic arc systems along the 23 S latitude of Chile and NW Argentina. In *Tectonics of the southern central Andes*, (pp. 141–153). Berlin Heidelberg: Springer.

Arkle, J. C., Armstrong, P. A., Haeussler, P. J., Prior, M. G., Hartman, S., Sendziak, K. L., & Brush, J. A. (2013). Focused exhumation in the syntaxis of the western Chugach Mountains and Prince William Sound, Alaska. *Geological Society of America Bulletin*, *125*, 776–793.

Avdievitch, N. N., Ehlers, T. A., & Glotzbach, C. (2018). Slow long-term exhumation of the West Central Andean plate boundary, Chile. *Tectonics*, *37*, 2243–2267. https://doi.org/10.1029/2017TC004944

Barnes, J. B., Ehlers, T. A., McQuarrie, N., O'sullivan, P. B., & Tawackoli, S. (2008). Thermochronometer record of central Andean Plateau growth, Bolivia (19.5 S). *Tectonics*, *27*, TC3003. https://doi.org/10.1029/2007TC002174

Bendick, R., & Ehlers, T. A. (2014). Extreme localized exhumation at syntaxes initiated by subduction geometry. *Geophysical Research Letters*, *41*, 5861–5867. https://doi.org/10.1002/2014GL061026

Benowitz, J. A., Haeussler, P. J., Layer, P. W., O'Sullivan, P. B., Wallace, W. K., & Gillis, R. J. (2012). Cenozoic tectono-thermal history of the Tordrillo Mountains, Alaska: Paleocene-Eocene ridge subduction, decreasing relief, and late Neogene faulting. *Geochemistry, Geophysics, Geosystems*, *13*, Q04009. https://doi.org/10.1029/2011GC003951

Benowitz, J. A., Layer, P. W., Armstrong, P., Perry, S. E., Haeussler, P. J., Fitzgerald, P. G., & VanLaningham, S. (2011). Spatial variations in focused exhumation along a continental-scale strike-slip fault: The Denali fault of the eastern Alaska Range. *Geosphere*, *7*, 455–467.

Billen, M. I. (2008). Modeling the dynamics of subducting slabs. *Annual Review of Earth and Planetary Sciences*, *36*, 325–356.

Bird, P. (1998). Testing hypotheses on plate-driving mechanisms with global lithosphere models including topography, thermal structure, and faults. *Journal of Geophysical Research*, *103*, 10,115–10,129.

Bird, P., Liu, Z., & Rucker, W. K. (2008). Stresses that drive the plates from below: Definitions, computational path, model optimization, and error analysis. *Journal of Geophysical Research*, *113*, B11406. https://doi.org/10.1029/2007JB005460

Brace, W. F., & Kohlstedt, D. L. (1980). Limits on lithospheric stress imposed by laboratory experiments. *Journal of Geophysical Research*, *85*, 6248–6252.

Brandon, M. T., Roden-Tice, M. K., & Garver, J. I. (1998). Late Cenozoic exhumation of the Cascadia accretionary wedge in the Olympic Mountains, northwest Washington State. *Geological Society of America Bulletin*, *110*, 985–1009.

Braun, J. (2003). Pecube: A new finite-element code to solve the 3D heat transport equation including the effects of a time-varying, finite amplitude surface topography. *Computers & Geosciences*, *29*, 787–794.

Braun, J., Thieulot, C., Fullsack, P., DeKool, M., Beaumont, C., & Huismans, R. (2008). DOUAR: A new three-dimensional creeping flow numerical model for the solution of geological problems. *Physics of the Earth and Planetary Interiors*, *171*, 76–91.

Braun, J., & Yamato, P. (2010). Structural evolution of a three-dimensional, finite-width crustal wedge. *Tectonophysics*, *484*(1-4), 181–192. https://doi.org/10.1016/j.tecto.2009.08.032

Brun, J. P. (2002). Deformation of the continental lithosphere: Insights from brittle-ductile models. *Geological Society, London, Special Publications*, *200*, 355–370.

Brun, J. P., Sokoutis, D., Tirel, C., Gueydan, F., Van den Driessche, J., & Beslier, M. O. (2018). Crustal versus mantle core complexes. *Tectonophysics*, *746*, 22–45. https://doi.org/10.1016/j.tecto.2017.09.017

Burov, E., Jolivet, L., Le Pourhiet, L., & Poliakov, A. (2001). A thermomechanical model of exhumation of high pressure (HP) and ultra-high pressure (UHP) metamorphic rocks in Alpine-type collision belts. *Tectonophysics*, *342*, 113–136.

Burov, E., & Yamato, P. (2008). Continental plate collision, P-T-t-z conditions and unstable vs. stable plate dynamics: Insights from thermo-mechanical modelling. *Lithos*, *103*, 178–204.

Burov, E. B. (2011). Rheology and strength of the lithosphere. *Marine and Petroleum Geology*, *28*, 1402–1443.

Burov, E. B., & Diament, M. (1995). The effective elastic thickness (Te) of continental lithosphere: What does it really mean? *Journal of Geophysical Research*, *100*(B3), 3905–3927. https://doi.org/10.1029/94JB02770

Buttles, J., & Olson, P. (1998). A laboratory model of subduction zone anisotropy. *Earth and Planetary Science Letters*, *164*, 245–262.

Byerlee, J. (1978). Friction of rocks. *Pure and Applied Geophysics*, *116*, 615–626.

Cailleau, B., & Oncken, O. (2008). Past forearc deformation in Nicaragua and coupling at the megathrust interface: Evidence for subduction retreat? *Geochemistry, Geophysics, Geosystems*, *9*, Q03016. https://doi.org/10.1029/2007GC001754

Capitanio, F. A., Faccenna, C., Zlotnik, S., & Stegman, D. R. (2011). Subduction dynamics and the origin of Andean orogeny and the Bolivian orocline. *Nature*, *480*, 83.

Capitanio, F. A., Morra, G., Goes, S., Weinberg, R. F., & Moresi, L. (2010). India-Asia convergence driven by the subduction of the Greater Indian continent. *Nature Geoscience*, *3*, 136–139.

Capitanio, F. A., & Replumaz, A. (2013). Subduction and slab breakoff controls on Asian indentation tectonics and Himalayan western syntaxis formation. *Geochemistry, Geophysics, Geosystems*, *14*, 3515–3531. https://doi.org/10.1002/ggge.20171

Carter, N. L., & Tsenn, M. C. (1987). Flow properties of continental lithosphere. *Tectonophysics*, *136*(1-2), 27–63. https://doi.org/10.1016/0040-1951(87)90333-7

Coblentz, D. D., & Richardson, R. M. (1996). Analysis of the South American intraplate stress field. *Journal of Geophysical Research*, *101*, 8643–8657.

Coblentz, D. D., Richardson, R. M., & Sandiford, M. (1994). On the gravitational potential of the Earth's lithosphere. *Tectonics*, *13*(4), 929–945. https://doi.org/10.1029/94TC01033

Crowley, J. L., Waters, D. J., Searle, M. P., & Bowring, S. A. (2009). Pleistocene melting and rapid exhumation of the Nanga Parbat massif, Pakistan: Age and P-T conditions of accessory mineral growth in migmatite and leucogranite. *Earth and Planetary Science Letters*, *288*, 408–420.

Currie, L., & Grist, A. M. (1996). Diachronous low temperature Paleogene cooling of the Alberni Inlet area, southern Vancouver Island, British Columbia: Evidence from apatite fission track analyses. Geological Survey of Canada Current Research, 119-125.

Duretz, T., Gerya, T. V., & Spakman, W. (2014). Slab detachment in laterally varying subduction zones: 3-D numerical modeling. *Geophysical Research Letters*, *41*, 1951–1956. https://doi.org/10.1002/2014GL059472

Ehlers, T. A. (2005). Computational tools for low-temperature thermochronometer interpretation. *Reviews in Mineralogy and Geochemistry*, *58*(1), 589–622. https://doi.org/10.2138/rmg.2005.58.22

England, P., & Molnar, P. (1990). Surface uplift, uplift of rocks, and exhumation of rocks. *Geology*, *18*(12), 1173–1177. https://doi.org/10.1130/0091-7613(1990)018<1173:SUUORA>2.3.CO;2

England, T. D. J., Currie, L. D., Massey, N. W. D., Roden-Tice, M. K., & Miller, D. S. (1997). Apatite fission-track dating of the Cowichan fold and thrust system, southern Vancouver Island, British Columbia. *Canadian Journal of Earth Sciences*, *34*(5), 635–645. https://doi.org/10.1139/e17-050

Enkelmann, E., Ehlers, T. A., Zeitler, P. K., & Hallet, B. (2011). Denudation of the Namche Barwa antiform, eastern Himalaya. *Earth and Planetary Science Letters*, *307*(3-4), 323–333. https://doi.org/10.1016/j.epsl.2011.05.004

Enkelmann, E., Piestrzeniewicz, A., Falkowski, S., Stübner, K., & Ehlers, T. A. (2017). Thermochronology in southeast Alaska and southwest Yukon: Implications for North American Plate response to terrane accretion. *Earth and Planetary Science Letters*, *457*, 348–358. https://doi.org/10.1016/j.epsl.2016.10.032

Enkelmann, E., Zeitler, P. K., Garver, J. I., Pavlis, T. L., & Hooks, B. P. (2010). The thermochronological record of tectonic and surface process interaction at the Yakutat-North American collision zone in southeast Alaska. *American Journal of Science*, *310*(4), 231–260. https://doi.org/10.2475/04.2010.01

Erdos, Z., Huismans, R. S., van der Beek, P., & Thieulot, C. (2014). Extensional inheritance and surface processes as controlling factors of mountain belt structure. *Journal of Geophysical Research: Solid Earth*, *119*, 9042–9061. https://doi.org/10.1002/2014JB011408

Faccenna, C., Bellier, O., Martinod, J., Piromallo, C., & Regard, V. (2006). Slab detachment beneath eastern Anatolia: A possible cause for the formation of the North Anatolian fault. *Earth and Planetary Science Letters*, *242*, 85–97.

Falkowski, S., Enkelmann, E., & Ehlers, T. A. (2014). Constraining the area of rapid and deep-seated exhumation at the St. Elias syntaxis, Southeast Alaska, with detrital zircon fission-track analysis. *Tectonics*, *33*, 597–616. https://doi.org/10.1002/2013TC003408

Ferguson, K. M., Armstrong, P. A., Arkle, J. C., & Haeussler, P. J. (2015). Focused rock uplift above the subduction décollement at Montague and Hinchinbrook Islands, Prince William Sound, Alaska. *Geosphere*, *11*, 144–159.

Ficini, E., Dal Zilio, L., Doglioni, C., & Gerya, T. V. (2017). Horizontal mantle flow controls subduction dynamics. *Scientific Reports*, *7*, 7550.

Gerya, T. V., Connolly, J. A., & Yuen, D. A. (2008). Why is terrestrial subduction one-sided? *Geology*, *36*, 43–46.

Gerya, T. V., Stern, R. J., Baes, M., Sobolev, S. V., & Whattam, S. A. (2015). Plate tectonics on the Earth triggered by plume-induced subduction initiation. *Nature*, *527*, 221–225.

Gerya, T. V., Yuen, D. A., & Maresch, W. V. (2004). Thermomechanical modelling of slab detachment. *Earth and Planetary Science Letters*, *226*, 101–116.

Goetze, C., & Evans, B. (1979). Stress and temperature in the bending lithosphere as constrained by experimental rock mechanics. *Geophysical Journal International*, *59*, 463–478.

Grove, T. L., Till, C. B., Lev, E., Chatterjee, N., & Médard, E. (2009). Kinematic variables and water transport control the formation and location of arc volcanoes. *Nature*, *459*, 694–697.

Gueydan, F., Morency, C., & Brun, J. P. (2008). Continental rifting as a function of lithosphere mantle strength. *Tectonophysics*, *460*, 83–93.

Gunnell, Y., Thouret, J. C., Brichau, S., Carter, A., & Gallagher, K. (2010). Low-temperature thermochronology in the Peruvian Central Andes: Implications for long-term continental denudation, timing of plateau uplift, canyon incision and lithosphere dynamics. *Journal of the Geological Society*, *167*, 803–815.

Haeussler, P. J., O'Sullivan, P., Berger, A. L., & Spotila, J. A. (2008). Neogene exhumation of the Tordrillo Mountains, Alaska, and correlations with Denali (Mount McKinley). In *Active tectonics and seismic potential of Alaska*, (Vol. 179, pp. 269–285).

Hayes, G. P., Wald, D. J., & Johnson, R. L. (2012). Slab1. 0: A three-dimensional model of global subduction zone geometries. *Journal of Geophysical Research*, *117*, B01302. https://doi.org/10.1029/2011JB008524

Heuret, A., & Lallemand, S. (2005). Plate motions, slab dynamics and back-arc deformation. *Physics of the Earth and Planetary Interiors*, *149*, 31–51.

Hirth, G., & Kohlstedt, D. (2003). Rheology of the upper mantle and the mantle wedge: A view from the experimentalists. In *Inside the subduction Factory*, (pp. 83–105).

Huismans, R. S., & Beaumont, C. (2002). Asymmetric lithospheric extension: The role of frictional plastic strain softening inferred from numerical experiments. *Geology*, *30*, 211–214.

Iwamori, H., Richardson, C., & Maruyama, S. (2007). Numerical modeling of thermal structure, circulation of H2O, and magmatism-metamorphism in subduction zones: Implications for evolution of arcs. *Gondwana Research*, *11*, 109–119.

Jadamec, M. A., & Billen, M. I. (2012). The role of rheology and slab shape on rapid mantle flow: Three-dimensional numerical models of the Alaska slab edge. *Journal of Geophysical Research*, *117*, B02304. https://doi.org/10.1029/2011JB008563

Jammes, S., & Huismans, R. S. (2012). Structural styles of mountain building: Controls of lithospheric rheologic stratification and extensional inheritance. *Journal of Geophysical Research*, *117*, B10403. https://doi.org/10.1029/2012JB009376

Johnson, S. Y., Zimmermann, R. A., Naeser, C. W., & Whetten, J. T. (1986). Fission-track dating of the tectonic development of the San Juan Islands, Washington. *Canadian Journal of Earth Sciences*, *23*, 1318–1330.

Juez-Larré, J., Kukowski, N., Dunai, T. J., Hartley, A. J., & Andriessen, P. A. (2010). Thermal and exhumation history of the Coastal Cordillera arc of northern Chile revealed by thermochronological dating. *Tectonophysics*, *495*, 48–66.

Kincaid, C., & Griffiths, R. W. (2003). Laboratory models of the thermal evolution of the mantle during rollback subduction. *Nature*, *425*, 58.

Kley, J., & Monaldi, C. R. (1998). Tectonic shortening and crustal thickness in the Central Andes: How good is the correlation? *Geology*, *26*, 723–726.

Kohlstedt, D. L., Evans, B., & Mackwell, S. J. (1995). Strength of the lithosphere: Constraints imposed by laboratory experiments. *Journal of Geophysical Research*, *100*, 17,587–17,602.

Koons, P. O., Hooks, B. P., Pavlis, T., Upton, P., & Barker, A. D. (2010). Three-dimensional mechanics of Yakutat convergence in the southern Alaskan plate corner. *Tectonics*, *29*, TC4008. https://doi.org/10.1029/2009TC002463

Koons, P. O., Zeitler, P. K., Chamberlain, C. P., Craw, D., & Meltzer, A. S. (2002). Mechanical links between erosion and metamorphism in Nanga Parbat, Pakistan Himalaya. *American Journal of Science*, *302*, 749–773.

Koons, P. O., Zeitler, P. K., & Hallet, B. (2013). Tectonic aneurysms and mountain building. In *Treatise on Geomorphology*, (Vol. 5, pp. 318–349).

Koptev, A., Burov, E., Calais, E., Leroy, S., Gerya, T., Guillou-Frottier, L., & Cloetingh, S. (2016). Contrasted continental rifting via plume-craton interaction: Applications to Central East African Rift. *Geoscience Frontiers*, *7*, 221–236.

Koptev, A., Burov, E., Gerya, T., Le Pourhiet, L., Leroy, S., Calais, E., & Jolivet, L. (2018). Plume-induced continental rifting and break-up in ultra-slow extension context: Insights from 3D numerical modeling. *Tectonophysics*, *746*, 121–137.

Koptev, A., Calais, E., Burov, E., Leroy, S., & Gerya, T. (2015). Dual continental rift systems generated by plume–lithosphere interaction. *Nature Geoscience*, *8*, 388.

Koptev, A., Calais, E., Burov, E., Leroy, S., & Gerya, T. (2018). Along-axis variations of rift width in a coupled lithosphere-mantle system, Application to East Africa. *Geophysical Research Letters*, *45*, 5362–5370. https://doi.org/10.1029/2018GL077276

Koptev, A. I., & Ershov, A. V. (2010). The role of the gravitational potential of the lithosphere in the formation of a global stress field. *Izvestiya Physics of the Solid Earth*, *46*, 1080–1094.

Lang, K. A., Huntington, K. W., Burmester, R., & Housen, B. (2016). Rapid exhumation of the eastern Himalayan syntaxis since the late Miocene. *Geological Society of America Bulletin*, *128*, 1403–1422.

Li, Z. H., Xu, Z., Gerya, T., & Burg, J. P. (2013). Collision of continental corner from 3-D numerical modeling. *Earth and Planetary Science Letters*, *380*, 98–111.

Liao, J., Gerya, T., Thielmann, M., Webb, A. A. G., Kufner, S. K., & Yin, A. (2017). 3D geodynamic models for the development of opposing continental subduction zones: The Hindu Kush-Pamir example. *Earth and Planetary Science Letters*, *480*, 133–146.

Lithgow-Bertelloni, C., & Guynn, J. H. (2004). Origin of the lithospheric stress field. *Journal of Geophysical Research*, *109*, B01408. https://doi.org/10.1029/2003JB002467

Liu, Z., & Bird, P. (2002a). Finite element modeling of neotectonics in New Zealand. *Journal of Geophysical Research*, *107*(B12), 2328. https://doi.org/10.1029/2001JB001075

Liu, Z., & Bird, P. (2002b). North America plate is driven westward by lower mantle flow. *Geophysical Research Letters*, *29*(24), 2164. https://doi.org/10.1029/2002GL016002

Mahadevan, L., Bendick, R., & Liang, H. (2010). Why subduction zones are curved. *Tectonics*, *29*, TC6002. https://doi.org/10.1029/2010TC002720

Maksaev, V., & Zentilli, M. (1999). Fission track thermochronology of the Domeyko Cordillera, northern Chile: Implications for Andean tectonics and porphyry copper metallogenesis. *Exploration and Mining Geology*, *8*, 65–90.

McInnes, B. I., Farley, K. A., Sillitoe, R. H., & Kohn, B. P. (1999). Application of apatite (U-Th)/He thermochronometry to the determination of the sense and amount of vertical fault displacement at the Chuquicamata porphyry copper deposit, Chile. *Economic Geology*, *94*, 937–947.

Menant, A., Sternai, P., Jolivet, L., Guillou-Frottier, L., & Gerya, T. (2016). 3D numerical modeling of mantle flow, crustal dynamics and magma genesis associated with slab roll-back and tearing: The eastern Mediterranean case. *Earth and Planetary Science Letters*, *442*, 93–107.

Michel, L., Ehlers, T. A., Glotzbach, C., Adams, B. A., & Stübner, K. (2018). Tectonic and glacial contributions to focused exhumation in the Olympic Mountains, Washington, USA. *Geology*, *46*, 491–494.

Moresi, L., Betts, P. G., Miller, M. S., & Cayley, R. A. (2014). Dynamics of continental accretion. *Nature*, *508*, 245–248.

Naliboff, J. B., Lithgow-Bertelloni, C., Ruff, L. J., & de Koker, N. (2012). The effects of lithospheric thickness and density structure on Earth's stress field. *Geophysical Journal International*, *188*, 1–17.

Nettesheim, M., Ehlers, T. A., Whipp, D., & Koptev, A. (2018). The influence of upper-plate advance and erosion on overriding plate deformation in orogen syntaxes. *Solid Earth*, *9*, 1207–1224.

Noury, M., Bernet, M., Schildgen, T. F., Simon-Labric, T., Philippon, M., & Sempere, T. (2016). Crustal-scale block tilting during Andean trench-parallel extension: Structural and geo-thermochronological insights. *Tectonics*, *35*, 2052–2069. https://doi.org/10.1002/2016TC004231

O'Sullivan, P. B., Murphy, J. M., & Blythe, A. E. (1997). Late Mesozoic and Cenozoic thermotectonic evolution of the central Brooks Range and adjacent North Slope foreland basin, Alaska: Including fission track results from the Trans-Alaska Crustal Transect (TACT). *Journal of Geophysical Research*, *102*, 20821–20845.

Pazzaglia, F. J., & Brandon, M. T. (2001). A fluvial record of long-term steady-state uplift and erosion across the Cascadia forearc high, western Washington State. *American Journal of Science*, *301*, 385–431.

Plafker, G., Nokleberg, W. J., & Lull, J. S. (1989). Bedrock geology and tectonic evolution of the Wrangellia, Peninsular, and Chugach terranes along the Trans-Alaska Crustal Transect in the Chugach Mountains and southern Copper River Basin, Alaska. *Journal of Geophysical Research*, *94*, 4255–4295.

Plunder, A., Thieulot, C., & Van Hinsbergen, D. J. (2018). The effect of obliquity on temperature in subduction zones: Insights from 3-D numerical modeling. *Solid Earth*, *9*, 759–776.

Pusok, A. E., Kaus, B. J., & Popov, A. A. (2018). The effect of rheological approximations in 3-D numerical simulations of subduction and collision. *Tectonophysics*, *746*, 296–311.

Pusok, A. E., & Kaus, B. J. P. (2015). Development of topography in 3-D continental-collision models. *Geochemistry, Geophysics, Geosystems*, *16*, 1378–1400. https://doi.org/10.1002/2015GC005732

Rajabi, M., Tingay, M., Heidbach, O., Hillis, R., & Reynolds, S. (2017). The present-day stress field of Australia. *Earth-Science Reviews*, *168*, 165–189.

Ranalli, G. (1995). *Rheology of the Earth*, (second ed.p. 413). London: Chapman and Hall.

Ranalli, G., & Murphy, D. C. (1987). Rheological stratification of the lithosphere. *Tectonophysics*, *132*, 281–295.

Reiners, P. W., Ehlers, T. A., Garver, J. I., Mitchell, S. G., Montgomery, D. R., Vance, J. A., & Nicolescu, S. (2002). Late Miocene exhumation and uplift of the Washington Cascade Range. *Geology*, *30*, 767–770.

Replumaz, A., Capitanio, F. A., Guillot, S., Negredo, A. M., & Villaseñor, A. (2014). The coupling of Indian subduction and Asian continental tectonics. *Gondwana Research*, *26*, 608–626.

Richardson, R. M., & Reding, L. M. (1991). North American plate dynamics. *Journal of Geophysical Research*, *96*, 12,201–12,223.

Roy, S. G., Koons, P. O., Upton, P., & Tucker, G. E. (2016). Dynamic links among rock damage, erosion, and strain during orogenesis. *Geology*, *44*, 583–586.

Ruh, J. B., Sallarès, V., Ranero, C. R., & Gerya, T. (2016). Crustal deformation dynamics and stress evolution during seamount subduction: High-resolution 3-D numerical modeling. *Journal of Geophysical Research: Solid Earth*, *121*, 6880–6902. https://doi.org/10.1002/2016JB013250

Russo, R. M., & Silver, P. G. (1996). Cordillera formation, mantle dynamics, and the Wilson cycle. *Geology*, *24*, 511–514.

Schellart, W. P., Freeman, J., Stegman, D. R., Moresi, L., & May, D. (2007). Evolution and diversity of subduction zones controlled by slab width. *Nature*, *446*, 308–311.

Schildgen, T. F., Ehlers, T. A., Whipp, D. M., Van Soest, M. C., Whipple, K. X., & Hodges, K. V. (2009). Quantifying canyon incision and Andean Plateau surface uplift, southwest Peru: A thermochronometer and numerical modeling approach. *Journal of Geophysical Research*, *114*, F04014. https://doi.org/10.1029/2009JF001305

Schildgen, T. F., Hodges, K. V., Whipple, K. X., Reiners, P. W., & Pringle, M. S. (2007). Uplift of the western margin of the Andean plateau revealed from canyon incision history, southern Peru. *Geology*, *35*, 523–526.

Silver, P. G., Russo, R. M., & Lithgow-Bertelloni, C. (1998). Coupling of South American and African plate motion and plate deformation. *Science*, *279*, 60–63.

Sobolev, S. V., & Babeyko, A. Y. (2005). What drives orogeny in the Andes? *Geology*, *33*, 617–620.

Spotila, J. A., Buscher, J. T., Meigs, A. J., & Reiners, P. W. (2004). Long-term glacial erosion of active mountain belts: Example of the Chugach-St. Elias Range, Alaska. *Geology*, *32*, 501–504.

Starke, J., Ehlers, T. A., & Schaller, M. (2017). Tectonic and climatic controls on the spatial distribution of denudation rates in Northern Chile (18° S to 23° S) determined from cosmogenic nuclides. *Journal of Geophysical Research: Earth Surface*, *122*, 1949–1971. https://doi.org/10.1002/2016JF004153

Stern, R. J., & Gerya, T. (2018). Subduction initiation in nature and models: A review. *Tectonophysics*, *746*, 173–198.

Sternai, P., Jolivet, L., Menant, A., & Gerya, T. (2014). Driving the upper plate surface deformation by slab rollback and mantle flow. *Earth and Planetary Science Letters*, *405*, 110–118.

Tesauro, M., Kaban, M. K., & Cloetingh, S. A. (2012). Global strength and elastic thickness of the lithosphere. *Global and Planetary Change*, *90*, 51–57.

Tesauro, M., Kaban, M. K., & Cloetingh, S. A. (2013). Global model for the lithospheric strength and effective elastic thickness. *Tectonophysics*, *602*, 78–86.

Tetreault, J. L., & Buiter, S. J. H. (2018). The influence of extension rate and crustal rheology on the evolution of passive margins from rifting to break-up. *Tectonophysics*, *746*, 155–172.

Thieulot, C., Fullsack, P., & Braun, J. (2008). Adaptive octree-based finite element analysis of two- and three-dimensional indentation problems. *Journal of Geophysical Research*, *113*, B12207. https://doi.org/10.1029/2008JB005591

Vogt, K., Matenco, L., & Cloetingh, S. (2017). Crustal mechanics control the geometry of mountain belts. Insights from numerical modelling. *Earth and Planetary Science Letters*, *460*, 12–21.

Vogt, K., Willingshofer, E., Matenco, L., Sokoutis, D., Gerya, T., & Cloetingh, S. (2018). The role of lateral strength contrasts in orogenesis: A 2D numerical study. *Tectonophysics*, *746*, 549–561.

Wada, I., Wang, K., He, J., & Hyndman, R. D. (2008). Weakening of the subduction interface and its effects on surface heat flow, slab dehydration, and mantle wedge serpentinization. *Journal of Geophysical Research*, *113*, B04402. https://doi.org/10.1029/2007JB005190

Whipp, D. M. Jr., Beaumont, C., & Braun, J. (2014). Feeding the "aneurysm": Orogen-parallel mass transport into Nanga Parbat and the western Himalayan syntaxis. *Journal of Geophysical Research: Solid Earth*, *119*, 5077–5096. https://doi.org/10.1002/2013JB010929

Whipp, D. M., Ehlers, T. A., Braun, J., & Spath, C. D. (2009). Effects of exhumation kinematics and topographic evolution on detrital thermochronometer data. *Journal of Geophysical Research*, *114*, F04021. https://doi.org/10.1029/2008JF001195

Willingshofer, E., & Sokoutis, D. (2009). Decoupling along plate boundaries: Key variable controlling the mode of deformation and the geometry of collisional mountain belts. *Geology*, *37*, 39–42.

Willingshofer, E., Sokoutis, D., Luth, S., Beekman, F., & Cloetingh, S. (2013). Subduction and deformation of the continental lithosphere in response to plate and crust-mantle coupling. *Geology*, *41*, 1239–1242.

Wipf, M., Zeilinger, G., Seward, D., & Schlunegger, F. (2008). Focused subaerial erosion during ridge subduction: Impact on the geomorphology in south-central Peru. *Terra Nova*, *20*, 1–10.

Wipf, M. A. (2006). Evolution of the Western Cordillera and Coastal Margin of Peru: Evidence from low-temperature thermochronology and geomorphology. PhD thesis, Swiss Federal Institute of Technology.

Wu, B., Conrad, C. P., Heuret, A., Lithgow-Bertelloni, C., & Lallemand, S. (2008). Reconciling strong slab pull and weak plate bending: The plate motion constraint on the strength of mantle slabs. *Earth and Planetary Science Letters*, *272*, 412–421.

Yamato, P., & Brun, J. P. (2017). Metamorphic record of catastrophic pressure drops in subduction zones. *Nature Geoscience*, *10*, 46–50.

Yang, T., & Gurnis, M. (2016). Dynamic topography, gravity and the role of lateral viscosity variations from inversion of global mantle flow. *Geophysical Journal International*, *207*, 1186–1202.

Yang, T., Gurnis, M., & Zahirovic, S. (2018). Slab avalanche-induced tectonics in self-consistent dynamic models. *Tectonophysics*, *746*, 251–265.

Zeitler, P. K., Meltzer, A. S., Brown, L., Kidd, W. S., Lim, C., & Enkelmann, E. (2014). *Tectonics and topographic evolution of Namche Barwa and the easternmost Lhasa block*, (Vol. 507, pp. 23–58). Tibet: Geological Society of America Special Papers.

Zeitler, P. K., et al. (2001). Erosion, Himalayan geodynamics, and the geomorphology of metamorphism. *GSA Today*, *11*, 4–9.